J. Fluid Mech. (2002), *vol.* 470, *pp.* 181–222.
DOI: 10.1017/S0022112002001787 Printed in the United Kingdom

Core–annular flow in a periodically constricted circular tube. Part 2. Nonlinear dynamics

By CHARALAMPOS KOURIS AND JOHN TSAMOPOULOS†

Laboratory of Computational Fluid Dynamics, Department of Chemical Engineering, University of Patras, Patras 26500, Greece

(Received 16 November 2000 and in revised form 29 May 2002)

Nonlinear dynamics of the concentric, two-phase flow of two immiscible fluids in a circular tube of variable cross-section is studied for parameter values where the steady core–annular flow (CAF) is linearly unstable. The simulations are based on a pseudo-spectral numerical method. They are carried out assuming axial symmetry, that the total flow rate remains constant and that all dependent variables are periodic in the axial direction, which includes the minimum necessary number of repeated units so that the obtained solution is independent of this number. The time integration originates with the numerically computed steady CAF or the steady CAF seeded with either the most unstable mode or random small disturbances. Only a limited number of the most interesting cases are presented. For the most part, the values of the majority of the dimensionless parameters are such that oil flows in the centre of the tube driven by an applied pressure gradient against gravity, whereas water is flowing in the annulus. It is shown that, whereas the steady (unstable) solution may indicate that the heavier water flows countercurrently with respect to the oil, the time periodic (observable) solution may indicate the same, albeit at a much smaller core flow rate or that concurrent flow occurs. This is due to the water being trapped between the large-amplitude interfacial waves that are generated and being convected by the oil. It is also shown that increasing the inverse Weber number increases the wave amplitude to the point that the flow of the core fluid may become discontinuous with a mechanism that depends on the viscosity ratio between the two fluids. Increasing the amplitude of the sinusoidal variation of the tube leads to a combination of travelling and standing waves, which interact to produce a time periodic solution with a long period associated with the time it takes the travelling wave to travel through the computational domain and a second much shorter period that is related to their interaction time. Qualitative agreement has been obtained upon comparing our numerical simulations with limited experimental reports, even though the experimental conditions were not identical to those in our model.

1. Introduction

There are a large number of technologically important applications where flow of two immiscible fluids takes place. One such example is the lubrication of oil by water. For the transportation of very viscous oil in pipelines, core–annular flow (CAF) can be an attractive alternative to heating or diluting the oil with its lightweight fractions. In lubricated CAF, the centrally flowing oil is surrounded by a less viscous fluid, such

† Author to whom correspondence should be addressed: tsamo@chemeng.upatras.gr

as water, which forms an annular layer. This flow pattern requires specific operating conditions, and reduces the pressure drop over the pipeline to almost the same order of magnitude as when only the less viscous fluid is present (Preziosi, Chen & Joseph 1989). In a second situation, two fluids flow concurrently through narrow passages in processes aimed at recovering oil from sedimentary rocks by injecting primarily water or steam. The displacing fluid follows the path of minimum resistance, that is, away from solid surfaces, and, usually, it does not remove the oil that adheres to corners and crevices in the rock. In a final example, concurrent two-phase flow of hydrogen and hydrocarbons takes place through millimetre-scale tortuous passages created by catalytic particles, which promote reforming oil and its byproducts in certain trickle bed reactors. In this case, the gas phase flows through the narrow flow paths, which are created by the catalytic particles, well wetted by oil, as they are packed inside the reactor. Unfortunately, the pores between sedimentary rocks and the interstices in packed beds do not provide a pathway of uniform cross-section and it is conceivable that this geometric non-uniformity may induce or modify already possible flow instabilities. It is well known that different flow regimes exist in a packed bed (trickling, pulsing, spray, etc.) and they affect greatly the reactor parameters, namely pressure drop, heat and mass transfer coefficients, reaction rate and liquid holdup. As a result, the prediction of the operating conditions leading to these flow regimes is critical in reactor design and operation. In fact, Kouris *et al.* (1998) showed that the effectiveness factors of the chemical reactions in hydrodesulphurization processes are greatly enhanced when the reactor operates in the pulsing flow regime owing to the increased average mass transfer coefficient of the gas phase.

When the assumption of a straight tube can be made, then there is analytical expression of the steady-state solution and, as a result, linear and weakly nonlinear stability analysis can be performed. More specifically, Hickox (1971) studied the stability of an axisymmetric, laminar, primary flow composed of two fluids flowing concentrically in a straight tube. He assumed that the fluids are incompressible with different viscosities and densities and examined the stability of the asymptotically long wavelength modes. His method was similar to the one used by Yih (1967) in investigating the effects of viscosity stratification in plane Couette and Poiseuille flows. Hickox (1971) concluded that, since instability is manifested however small the Reynolds numbers, turbulence is not expected as an end result of instability. He further anticipated that the exponential growth would not continue beyond the linear regime, but that finite-amplitude waves are possible. Hooper & Boyd (1983) examined the stability of the concurrent plane Couette flow of two superposed viscous fluids in an infinite region neglecting surface tension. They showed that this flow is unstable to short-wavelength disturbances. Hooper (1989) examined the problem when the lower fluid is of finite depth bounded below by a solid boundary, while the upper fluid is of infinite extent. In that case, the flow is unstable when the lower fluid is also the more viscous one and stable otherwise. Yiantsios & Higgins (1988) extended the analysis performed by Yih (1967) examining the stability to disturbances of any wavelength. They have identified not only the long-wavelength unstable modes reported by Yih, but also short-wavelength unstable modes which arise with increasing *Re* and are associated with Tollmien–Schlichting waves. The characteristic of Tollmien–Schlichting waves in a single-phase flow with a free surface is that they are stable according to Rayleigh's inviscid criterion for capillary instability, but they are unstable at sufficiently large Reynolds number (Drazin & Reid 1981). Preziosi, Chen & Joseph (1989) have studied extensively the linear stability of the axisymmetric core–annular flow by varying the viscosity and volume ratios of the two fluids, the Reynolds and the

Ohnesorge numbers. They have verified that this flow is generally unstable, except when the annular region is occupied by the less viscous fluid, it is sufficiently thin and the Reynolds number varies within a limited range which depends on the other flow and fluid parameters.

The weakly nonlinear dynamics of the concentric fluid arrangement in a straight tube was studied first by Hammond (1983) who assumed a base state with static fluids and that the annular fluid is thin. Hammond used the long-wave approximation and derived an evolution equation of the interface, which predicted film rupture, when it was solved beyond the limits of validity of the linear analysis. Subsequently, Frenkel *et al.* (1987) examined the stability of Poiseuille flow of two fluids, which were assumed to have equal properties leaving only surface tension to act on them, but retained the previous geometrical restriction. This leads to decoupling the flow in the core from the flow in the annular film. The dynamics of the interface were determined by the Kuramoto–Sivashinsky equation with both stabilizing and destabilizing terms related to surface tension and a nonlinear term related to the base flow; the coupling of these terms leads to growth and subsequent saturation of initial disturbances. In particular, they identified in their film evolution equation the second derivative of the interface with respect to the axial distance as inducing the usual capillary instability, sinusoidal at inception. As this deformation increases, nonlinear convection induces asymmetry and steepening of the wave, but then, the fourth derivative of the interface with respect to the axial distance, arising from the curvature operator, becomes important and prevents breakup. Papageorgiou, Maldarelli & Rumschitzki (1990), have assumed pressure-driven CAF in a straight tube, making an effort to include the dynamics of both phases, and have obtained numerical solutions to their final model equations. Their equations are augmented versions of the Kuramoto–Sivashinsky equation with integral terms arising from the flow in the core and capture the weakly nonlinear evolution of the perfect CAF. Kerchman (1995) has extended the previous analysis by removing the constraint that the deviation of the interface from its initial value is smaller than the thickness of the annular film, assuming instead, that interfacial shear is negligible. The fully nonlinear dynamics of CAF have been examined, Li & Renardy (1999) and Kouris & Tsamopoulos (2001*b*, 2002), by solving the axisymmetric Navier–Stokes equations in both space and time. They have examined the effect of the Reynolds number, the surface tension and the viscosity ratio. In the first two reports, assuming that oil flows in the core and water in the annulus, interfacial waveforms were computed, which have a 'bamboo' shape; the speed and the wavelength of which are very well correlated with linear stability theory as well as with experiments. In the third report, the less viscous fluid is centrally located giving rise to 'sawtooth' waves with wavelength, amplitude and other characteristics that depend on fluid properties and flow conditions.

On the other hand, when the tube radius depends on the axial distance, the steady-state solution does not admit an analytical solution and both components of the velocity vector (axial and radial) of either fluid depend on the axial and the radial distance. In order to capture the most unstable mode of the governing equations a fully coupled eigenvalue problem must be solved, in contrast to the straight-tube case. In a straight tube, the axial dependence of the eigenvector is known beforehand and thus, only a one-dimensional eigenvalue problem, in the radial direction, should be solved for every axial wavenumber. For this reason, even the linear stability of CAF in a constricted tube was not thoroughly examined until recently. Kouris & Tsamopoulos (2000, 2001*a*), assuming moderate constriction ratios with and without

employing the lubrication approximation, have examined how the neutral stability curves depend on the effect of surface tension, which is measured either by the inverse Weber number or the inverse Ohnesorge number, the Reynolds number, the viscosity and density ratios of the two fluids as well as the volume fraction of the core fluid. They have also examined the effect of gravity when the two fluids are of different densities and the effect of the number of unit cells that comprise the undulating tube. The weakly nonlinear stability analysis of CAF in an undulating tube is still lacking. Kouris & Tsamopoulos (2000) have integrated, in both space and time, a simplified set of equations derived using the lubrication approximation. However, because of this approximation they focused their attention only to small *Re*, moderate constriction ratio and viscosity and density ratios close to unity, i.e. close to the neutral stability curves. Thus, they have verified that the unstable interfacial modes, after experiencing an exponential growth in time, finally saturate giving rise in this way to finite-amplitude interfacial waves.

Here, we present the solution of the axisymmetric time-dependent Navier–Stokes equations, relaxing in this way the lubrication approximation and examining thoroughly the effect of various parameters in the time evolution of CAF in constricted tubes deep into the unstable domain, i.e. away from the corresponding neutral curve (Kouris & Tsamopoulos 2001*a*). More specifically, we examine the effect of the Reynolds number assuming the physical properties that correspond to the oil/water CAF assuming that the ratio of the minimum to the maximum radius of the tube is equal to either 0.8 or 0.9. For the same values of the physical properties and in a straight tube, the so-called 'bamboo' waves arise (Li & Renardy 1999; Kouris & Tsamopoulos 2001*b*). This type of wave is an axially travelling one, characterized by sharp crests, flat troughs and a constant wave speed. These structures are well documented in the experiments of Bai, Chen & Joseph (1992). We also examine the effect of the other parameters such as viscosity ratio, Froude number and surface tension. When surface tension takes large values, the resulting waves have a 'sawtooth' shape and increasing it further causes breakup of the fluid/fluid interface. On the other hand, the viscosity ratio cannot take values much larger than unity, because then the interface tends to break up more readily, which cannot be accommodated by the otherwise most efficient solution method we have chosen.

The remainder of this paper is organized as follows. The governing equations, which depend on nine dimensionless parameters: the Reynolds, Weber and Froude numbers, the ratios of density, viscosity and volume of the two liquids as well as the constriction and aspect ratios and the number of unit cells, are presented in § 2. Results and discussion are given in § 3, § 4 and § 5, comparison with available experiments is made in § 6 and conclusions are drawn in § 7.

2. Governing equations

We examine the incompressible axisymmetric core–annular flow (CAF) of two Newtonian fluids in an undulating tube of circular cross-section, as shown in figure 1. In what follows, we use the symbol $\hat{}$ to denote dimensional quantities, $\hat{t}$ to denote the time variable and $\boldsymbol{e}_r$, $\boldsymbol{e}_\theta$ and $\boldsymbol{e}_z$ to denote the unit normal vectors of the cylindrical coordinate system $(\hat{r}, \hat{\theta}, \hat{z})$, respectively. The radius of the tube, $\hat{R}_2$, varies sinusoidally between the maximum, $\hat{R}_{max}$, and the minimum, $\hat{R}_{min}$, value within the axial distance $\hat{L}$, and the number of the unit cells that comprises the computational domain is denoted by N. The axial variation of the radius of the tube is described by the

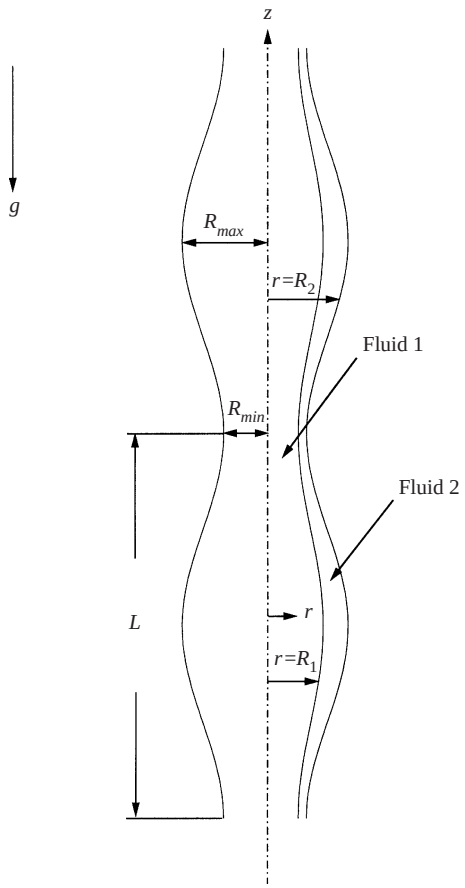

FIGURE 1. Schematic presentation of the flow geometry composed of two unit cells, showing the tube wall and the fluid/fluid interface.

following equation:

$$\hat{R}_2(\hat{z}) = \frac{\hat{R}_{max} + \hat{R}_{min}}{2} - \frac{\hat{R}_{max} - \hat{R}_{min}}{2} \cos\left(\frac{2\pi\hat{z}}{\hat{L}}\right), \quad (0 \leqslant \hat{z} \leqslant N\hat{L}). \tag{2.1}$$

The centreline of the pipe is located at $\hat{r} = 0$, the region $0 \leqslant \hat{r} \leqslant \hat{R}_1(\hat{z}, \hat{t})$ is occupied by the core fluid (fluid 1) with viscosity and density $(\hat{\mu}_1, \hat{\rho}_1)$, whereas the annular fluid (fluid 2) with viscosity and density $(\hat{\mu}_2, \hat{\rho}_2)$ is located in the region $\hat{R}_1(\hat{z}, \hat{t}) \leqslant \hat{r} \leqslant \hat{R}_2(\hat{z})$. The position vector of the fluid/fluid interface is:

$$\hat{\boldsymbol{R}}_1 = \boldsymbol{e}_r \hat{R}_1(\hat{z}, \hat{t}) + \boldsymbol{e}_z \hat{z}. \tag{2.2}$$

The radial and axial components of the axisymmetric velocity vector of each fluid are denoted by:

$$\hat{\boldsymbol{U}}_i = (\hat{U}_i, 0, \hat{W}_i) = \boldsymbol{e}_r \hat{U}_i + \boldsymbol{e}_\theta 0 + \boldsymbol{e}_z \hat{W}_i. \tag{2.3}$$

The equations that govern the motion of both fluids are the mass, equation (2.4), and

momentum, equation (2.5), balances of either phase

$$\nabla \cdot \hat{\boldsymbol{U}}_i = 0, \tag{2.4}$$

$$\hat{\rho}_i \left(\frac{\partial \hat{\boldsymbol{U}}_i}{\partial \hat{t}} + \hat{\boldsymbol{U}}_i \cdot \nabla \hat{\boldsymbol{U}}_i \right) = -\nabla \hat{P}_i + \nabla \cdot \hat{\boldsymbol{\tau}}_i - \hat{\rho}_i g \boldsymbol{e}_z, \tag{2.5}$$

where gravity acts along the axis of the tube to retain the axial symmetry, downward, in the $-\boldsymbol{e}_z$ direction and against the flow of the core fluid. The stress tensor of each Newtonian fluid, i, is defined by $\hat{\boldsymbol{\tau}}_i = \hat{\mu}_i(\nabla \hat{\boldsymbol{U}}_i + \nabla \hat{\boldsymbol{U}}_i^T)$. The kinematic condition, equation (2.6), governs the motion of the fluid/fluid interface:

$$\frac{\partial \hat{\boldsymbol{R}}_1}{\partial \hat{t}} + \hat{\boldsymbol{U}}_i \cdot \nabla \hat{\boldsymbol{R}}_1 = \hat{\boldsymbol{U}}_i(\hat{R}_1(\hat{z}, \hat{t}), \hat{z}, \hat{t}). \tag{2.6}$$

The axisymmetric set of equations (2.4)–(2.6) are solved subject to the following boundary conditions in the radial direction:

$$\hat{U}_1 = \frac{\partial \hat{W}_1}{\partial \hat{r}} = 0 \quad \text{on} \quad \hat{r} = 0, \tag{2.7}$$

$$\hat{\boldsymbol{U}}_2 = \boldsymbol{0} \quad \text{on} \quad \hat{r} = \hat{R}_2(\hat{z}), \tag{2.8}$$

$$\| \hat{\boldsymbol{U}} \| = \boldsymbol{0} \quad \text{on} \quad \hat{r} = \hat{R}_1(\hat{z}, \hat{t}), \tag{2.9}$$

$$(-\| \hat{P} \| - 2H\hat{T})\boldsymbol{n} + \| \hat{\boldsymbol{\tau}} \| \cdot \boldsymbol{n} = \boldsymbol{0} \quad \text{on} \quad \hat{r} = \hat{R}_1(\hat{z}, \hat{t}). \tag{2.10}$$

The above boundary conditions state that: the velocity field remains bounded at the centreline, (2.7); zero at the solid wall, (2.8); continuous across the fluid/fluid interface, (2.9); whereas the interfacial forces exerted by either phase balance each other in the direction tangent to the interface and balance capillarity in the direction normal to it, (2.10). In this balance, $-2H = \nabla \cdot \boldsymbol{n}|_{r=\hat{R}_1}$ is twice the mean surface curvature of the fluid/fluid interface and $\hat{T}$ is the coefficient of the interfacial tension. The unit vectors normal and tangent to the surface $\hat{r} = \hat{R}_1(\hat{z}, \hat{t})$ are denoted by $\boldsymbol{n}$, and $\boldsymbol{t}$, respectively, with the normal vector pointing from fluid 1 to fluid 2. By $\| \cdot \| = (\cdot)_1 - (\cdot)_2$ is denoted the jump of the bracketed quantity over the interface $\hat{r} = \hat{R}_1(\hat{z}, \hat{t})$. In the axial direction, we impose that the velocity field, the stress tensor of both fluids as well as the fluid/fluid interface are periodic functions with period the length of the computational domain, $N\hat{L}$. In addition to the previous boundary conditions, and so that the set of equations (2.4)–(2.6) is well defined, we impose that the volume fraction of the core fluid and the total volumetric flow rate of both phases remain constant in time. These conditions are imposed instead of the volumetric flow rate of each phase separately. The latter are inconsistent with the periodicity that we impose between the two ends of the tube and the expected time-periodic solution, and so they give non-converging or physically unrealistic solutions.

Equations (2.4)–(2.6) together with the boundary conditions (2.7)–(2.10) are made dimensionless by scaling the radial coordinate with the maximum radius of the tube $\hat{R}_{max}$ and the axial coordinate with the length $\hat{L}/2\pi$. The characteristic velocity in the axial direction $\hat{W}_o$ is chosen so that the total dimensionless volumetric flow rate of both fluids equals unity, that is,

$$\hat{W}_o = \frac{1}{\hat{R}_{max}^2} \left(\int_0^{\hat{R}_1} \hat{r} \hat{W}_1 \, \mathrm{d}\hat{r} + \int_{\hat{R}_1}^{\hat{R}_2} \hat{r} \hat{W}_2 \, \mathrm{d}\hat{r} \right). \tag{2.11}$$

It can be shown easily that $\hat{W}_o$ is half the average velocity computed at the axial distance where the radius of the tube is maximized. The pressure as well as the components of the stress tensor of each fluid are made dimensionless using the inertial pressure scale $\hat{\rho}_1 \hat{W}_o{}^2$, whereas time is scaled using the time required by both fluids to travel the characteristic axial length given the adopted velocity $\hat{W}_o$, i.e. $\hat{L}/2\pi\hat{W}_o$. The resulting set of equations is solved in the streamfunction–vorticity formulation and the characteristic values of the streamfunction and of the vorticity are $\hat{W}_o \hat{R}_{max}^2$ and $\hat{W}_o/\hat{R}_{max}$, respectively. After introducing the above scales into (2.1)–(2.10), nine dimensionless numbers appear. The geometry is characterized by the constriction ratio $\alpha = R_{min}/R_{max}$, the aspect ratio $\Lambda = 2\pi\hat{R}_{max}/\hat{L}$ and the number of the unit cells N. The physical properties of both fluids as well as the flow field give rise to the following six dimensionless numbers: the viscosity ratio $\mu = \hat{\mu}_2/\hat{\mu}_1$; the density ratio $\rho = \hat{\rho}_2/\hat{\rho}_1$; the Reynolds number $Re = \Lambda\hat{\rho}_1\hat{R}_{max}\hat{W}_o/\hat{\mu}_1$; the inverse Weber number $W = \hat{T}(\hat{\rho}_1\hat{W}_o^2\hat{R}_{max})$; the inverse Froude number $F = (\rho - 1)g\hat{R}_{max}/(\Lambda\hat{W}_o^2)$ and the core volume fraction $V = \hat{V}_C/\hat{V}_T$ which is defined as the ratio of the volume occupied by the core fluid $\hat{V}_C$ to the total internal volume of the tube $\hat{V}_T$. It is worth mentioning that gravity enters the problem through the density difference between the two fluids. The effective gravity parameter F is introduced only in the equations of motion of the annular fluid and not in those of the core fluid, since its effect on the core fluid is incorporated in the definition of the generalized pressure variable, which is composed of the usual pressure term and the hydrostatic variation of the pressure in the bulk of the core fluid.

In order to solve numerically the above time-dependent partial differential equations, we transform them by introducing the streamfunction and the vorticity of each fluid and then we employ the following non-orthogonal body-fitted coordinate transformation $(r, z, t) \rightarrow (x_1, x_2, \tau)$.

$$\text{Domain of core fluid:} \qquad x_1 = 1 - 2\frac{r}{R_1(z,t)}, \quad x_2 = z, \quad \tau = t, \tag{2.12}$$

$$\text{Domain of annular fluid:} \qquad x_1 = -1 + 2\frac{r - R_1(z,t)}{R_2(z) - R_1(z,t)}, \quad x_2 = z, \quad \tau = t. \tag{2.13}$$

This normalization is essential in order to transform the boundaries of the regions that each fluid occupies to coordinate lines in the new transformed space, given the spectral method of solution that we have adopted and in order to correctly discretize the physical domain. The bounds of the new independent variables are the following:

$$-1 \leqslant x_1 \leqslant 1, \quad 0 \leqslant x_2 \leqslant 2\pi N, \quad \tau \geqslant 0 \tag{2.14}$$

We approximate every dependent variable using Chebyshev polynomials and Fourier modes in the x_1 and x_2 directions, respectively, whereas the grid points in these directions are defined by the following relationships:

$$x_{1_k} = \cos\left(\pi\frac{k}{K}\right), \quad (0 \leqslant k \leqslant K), \qquad x_{2_l} = \frac{2\pi l}{L+1}, \quad (0 \leqslant l \leqslant L) \tag{2.15}$$

where $K(L)$ is the highest-order Chebyshev polynomial (Fourier mode) that we use. Every dependent variable in the transformed space is approximated as a sum of

products of Chebyshev polynomials and Fourier modes, that is,

$$f(x_1, x_2, \tau) = \sum_{i=0}^{K} \sum_{j=0}^{L} a_{ij}(\tau)\ C_i(x_1)\ F_j(x_2). \tag{2.16}$$

The derivative of each function in (2.16), is evaluated by differentiating term by term its spectral expansion, whereas the unknown functions, $a_{ij}(\tau)$, are evaluated by exactly satisfying the differential equations at the collocation points and at every time step. By using K and L collocation points in the radial and axial direction, respectively, the total number of unknowns are $4KL + L$ where KL are the unknowns of either the streamfunction or the vorticity equation in each phase and L is the number of unknowns of the interface. Owing to the fairly complicated form of the governing equations, the Jacobian matrix is formed numerically using one-sided finite differences. We have found that, when the tube is composed of one unit cell, 65 Fourier and 13 Chebyshev modes are adequate to resolve the flow field of both fluids, whereas, when the tube is composed of two unit cells, 111 Fourier and 11 Chebyshev modes are required. The time integration is performed using the implicit, second-order accurate, Adams–Moulton method with constant time step of typical size 0.5×10^{-3}. The size of the time step was chosen in order to guarantee accuracy (after performing a number of numerical experiments) without increasing the computational cost very much. In order to reduce the time required to compute the solution at each time step, we adopt the modified Newton–Raphson technique. According to it, we use the LU-decomposed Jacobian matrix from a previous time step in order to find the solution at the current time step and we update it only when the number of iterations exceeds 200. Additional information concerning the choice and other details of the numerical method of solution, its convergence rate as well as comparison of linear with nonlinear results can be found in Kouris *et al.* (2002). A typical calculation required about 10 days of CPU time in an ALPHA-DEC DS-20 machine with two processors.

Generally, our time-dependent calculations are initialized as follows. First, we compute the steady solution given the dimensionless numbers and, then, this steady state is used as initial condition to the initial-boundary-value problem. In all examined cases, an independent stability analysis of the steady solution has been performed in order to determine whether the steady solution is linearly unstable and how well the linear temporal frequencies are correlated with those predicted dynamically.

3. Large constriction ratio ($a = 0.9$): effect of Re on oil–water upflow

In this first set of three dynamic simulations we use values of the dimensionless numbers that correspond to the case where oil flows in the core and water in the annulus. More specifically, we use the physical properties for these two fluids reported by Bai *et al.* (1992), who conducted experiments of CAF in a straight tube. We assume that the viscosity and the density of oil are $\hat{\mu}_1 = 6.01$ poise and $\hat{\rho}_1 = 0.905\,\mathrm{g\,cm^{-3}}$, respectively, whereas the properties of water are $\hat{\mu}_2 = 0.01$ poise and $\hat{\rho}_2 = 0.995\,\mathrm{g\,cm^{-3}}$. The coefficient of interfacial tension of this pair of fluids is $\hat{T} = 8.54\,\mathrm{dyn\,cm^{-1}}$. Using these properties, we compute the viscosity and the density ratios of the two fluids, which are equal to 0.00166 and 1.09945, respectively. Assuming that the acceleration due to gravity is $g = 981\,\mathrm{cm\,s^{-2}}$ we compute the Galileo Ga and the inverse Ohnesorge

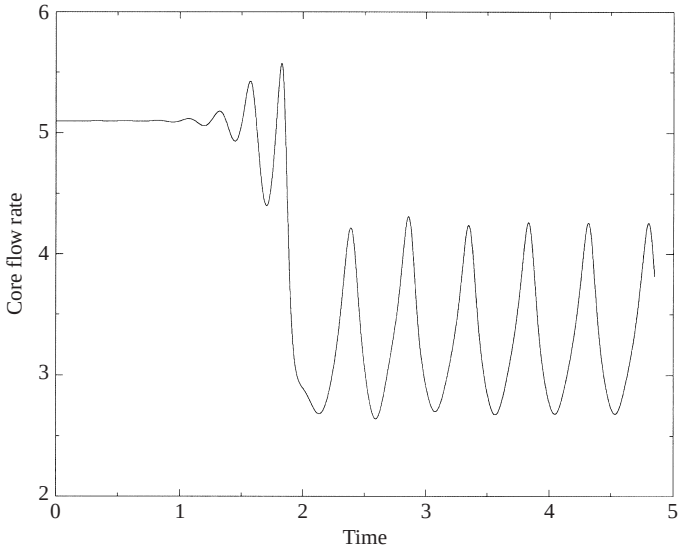

FIGURE 2. Time evolution of the core flow rate
$(\alpha, \Lambda, N, V, \mu, \rho, Re, W, F) = (0.9, 1, 1, 0.553, 0.00166, 1.09945, 0.01, 1020, 2389.6)$.

J numbers using the following relationships:

$$Ga = \left(\frac{\hat{\rho}_1}{\hat{\mu}_1}\right)^2 \hat{R}_2^3 g = 2.4028, \quad J = \frac{\hat{\rho}_1 \hat{T} \hat{R}_2}{\hat{\mu}_1^2} = 0.102. \tag{3.1}$$

The benefit of setting the values of these dimensionless numbers is that they depend only on the physical properties of the fluids in contrast to W and F, which also depend on the characteristic velocity. By combining J and Ga with Re, we can compute the inverse Weber and the inverse Froude numbers as follows:

$$W = J(\Lambda/Re)^2, \qquad F = Ga(\rho - 1)\Lambda/Re^2. \tag{3.2}$$

So, in the first three numerical experiments, we have varied Re, while keeping Ga and J constant. More specifically, in all three cases, we have set $(\alpha, \Lambda, N, \mu, \rho, J, Ga, V) = (0.9, 1, 1, 0.00166, 1.09945, 0.102, 2.4028, 0.553)$ and varied Re. The dimensionless numbers that characterize the geometry correspond to an undulating tube positioned vertically with the core fluid flowing upwards against gravity. The computational domain is composed of one cell with its minimum radius only 0.9 times its maximum radius, while its length is approximately 6.28 times its maximum radius. It is worth pointing out that for the present values of the physical parameters, the perfect CAF in a straight tube is unstable and the waveform that results after saturation of the instability resembles the 'bamboo' shape; (see Bai, Kelkar & Joseph 1996; Li & Renardy 1999; Kouris & Tsamopoulos 2001*b*). The goal of this analysis, in addition to investigating the effect of the various dimensionless numbers on the CAF in a constricted tube, is to find out whether this new geometry interferes with the above mentioned waves and, if it does, in which way it modifies them.

3.1. *Core fluid with small Reynolds number* ($Re = 0.01$, *case 1*)

Figures 2 and 3 correspond to $Re = 0.01$, while using relationships (3.1)–(3.2) the inverse Weber and the inverse Froude numbers are found to be equal to 1020 and 2389.6, respectively. The unstable eigenvalues of the steady solution that corresponds

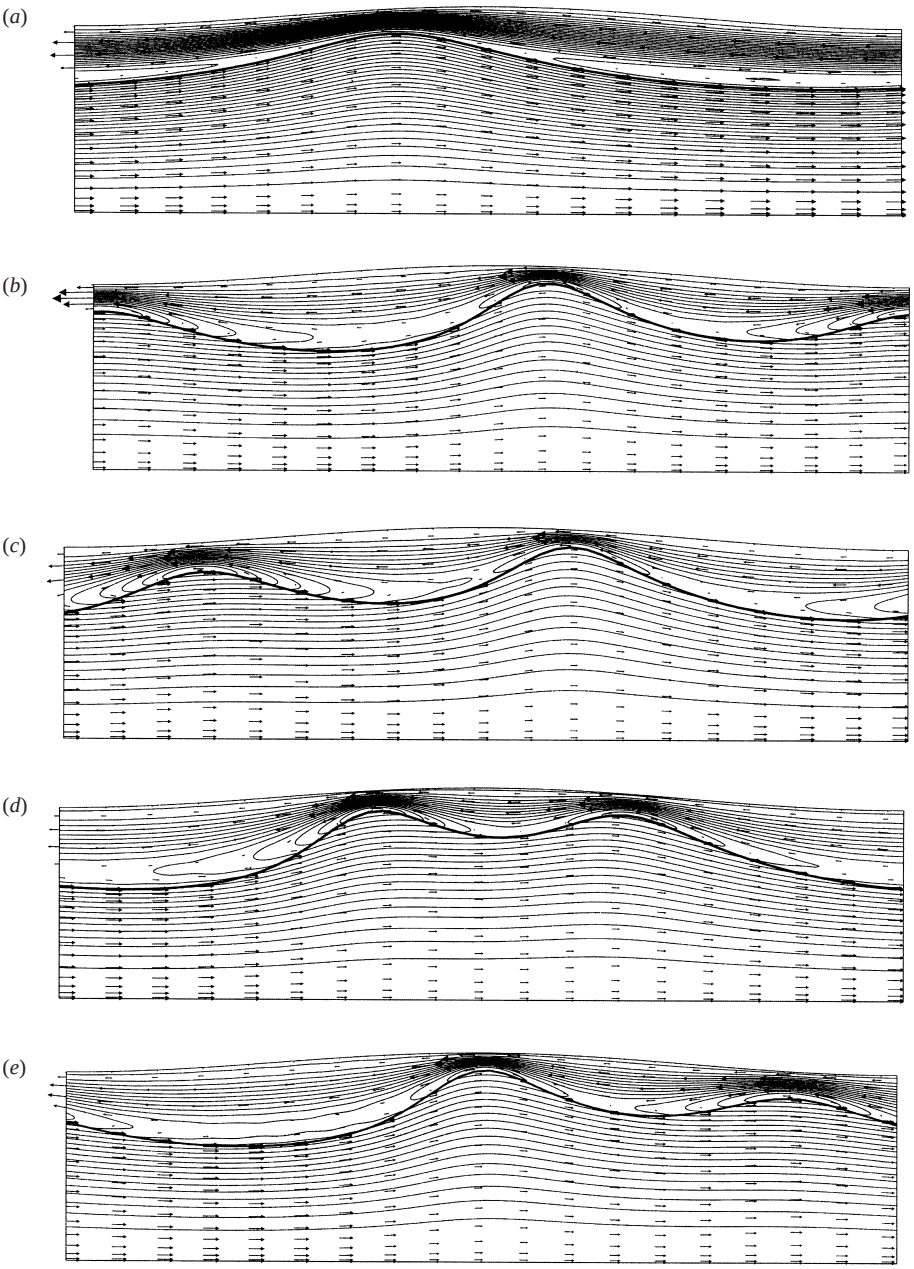

FIGURE 3. Flow fields that correspond to (*a*) the steady solution, (*b*) $t = 4.313$, (*c*) $t = 4.403$, (*d*) $t = 4.533$ (*e*) $t = 4.703$ $(\alpha, \Lambda, N, V, \mu, \rho, Re, W, F) = (0.9, 1, 1, 0.553, 0.00166, 1.09945, 0.01, 1020, 2389.6)$. In this and in all subsequent figures the mean flow direction is to the right and (except for figures 13 and 14) gravity points to the left.

to the above values of the dimensionless numbers together with those for the next two cases are shown in table 1. Since two modes have eigenvalues with positive real parts, the steady flow is unstable and, thus, physically unrealizable.

Figure 2 and the similar figures that are presented hereinafter show the time evolution of the core flow rate Q_1 computed at the tube entrance, which is taken

	Unstable eigenvalues		
Number	Case 1	Case 2	Case 3
1	5.702 ± 25.07i	0.869 ± 1.819i	0.6228 ± 2.287i
2	2.349 ± 50.03i	1.523 ± 7.702i	1.017 ± 6.366i
3	—	1.281 ± 13.37i	0.9728 ± 10.57i
4	—	0.639 ± 18.93i	0.7032 ± 14.77i
5	—	—	0.3489 ± 18.90i

TABLE 1. Unstable eigenvalues for $(\alpha, \Lambda, N, \mu, \rho, J, Ga, V) = (0.9, 1, 1, 0.00166, 1.09945, 0.102, 2.4028, 0.553)$; and case 1: $Re = 0.01$, $W = 1020$, $F = 2389.6$; case 2: $Re = 0.1$, $W = 10.2$, $F = 23.9$; case 3: $Re = 0.25$, $W = 1.632$, $F = 3.823$.

to be at the minimum tube radius. The computation of the instantaneous core flow rate at a certain axial distance is not representative of its values for the whole domain as this function, in addition to being time dependent, is also dependent on the axial distance at which it is computed. However, we use this function as a tool in order to identify instability, to compute temporal frequencies and to identify whether instability has fully saturated. When conclusions are drawn with regard to the core flow rate corresponding to a time periodic solution, the core flow rate averaged in the axial distance, $\langle Q_1 \rangle$, as well as averaged in both the axial distance and time $\{Q_1\}$, are computed too. Figure 2 shows that the flow departs from the linearly unstable steady solution, which is used as initial condition, and after a short transient ($t < 2.1$) reaches an oscillatory state of constant amplitude, i.e. a stable limit cycle. In this case, Q_1 varies between the values 2.682 and 4.258, with $\{Q_1\} = 3.28$, and the core flow rate that corresponds to the steady solution is equal to 5.098. The oil flow rate in figure 2 takes values above unity, although we impose a value of 1 on the total dimensionless flow rate, because oil and water flow countercurrently. This results in a positive volumetric flow rate for the oil and a negative volumetric flow rate for the water and thus, the oil flow rate is above unity compensating for the negative flow rate of the water. The fact that $\{Q_1\}$ is smaller than its value for the steady solution ($3.28 < 5.098$) coupled with the fact that the volume which each fluid occupies inside the tube is constant and, thus, the average flow cross-section of either phase is constant too, leads to the conclusion that the mean core velocity is smaller in the nonlinear regime than in the perfect CAF. In particular, the mean core velocity in the nonlinear regime is reduced by more than 35% compared to that for the steady solution. This conclusion is also in accordance with results obtained by Li & Renardy (1999) and Kouris & Tsamopoulos (2001*b*), who have studied the nonlinear dynamics of the CAF in a straight tube for similar values of the dimensionless numbers, albeit for concurrent flow only. They have reported that the inception of instability and its subsequent saturation, which gives rise to 'bamboo' waves, leads to a considerable decrease in both the mean core velocity and the holdup ratio, i.e. the ratio of the mean residence time of the annular fluid to that of the core (see also Joseph & Renardy 1993).

Using figure 2, we compute the temporal oscillation frequency, which is 24.933, well before the abrupt transition from the linear to the nonlinear regime ($t \sim 1$) and becomes 12.928 after saturation. The comparison of these values with the results presented in table 1 shows that although the graphically computed linear frequency approaches quite well that using the linear theory (eigenvalue 1 in table 1) within an error 0.5% only, the linear frequency is twice as large as the nonlinear one. Although

the linear theory is not expected to predict fully nonlinear phenomena accurately, especially when the system is far from the initial state for which the eigenvalues have been computed, such a large deviation is puzzling. Moreover, Kouris & Tsamopoulos (2000, 2001*b*, 2002) found that the nonlinear temporal frequency in all cases does not deviate considerably from the linear one. What has changed between those cases and here is that now we deal with counterflow of the two phases. The bifurcating travelling waves saturate at large amplitudes, which in turn are strongly affected by the sinusoidally varying solid wall and, thus, the linear results become inaccurate.

Figure 3(*a*) shows the flow field that corresponds to the steady solution. The fluid/fluid interface is denoted by a thicker line, and the velocity vectors are plotted in addition to the streamlines. The velocity vectors, which are always tangent to the computed streamlines, give us a clear indication of the intensity of the flow field, something which cannot be visualized otherwise. The value of the streamfunction at the solid wall is equal to 0, whereas that at the centreline is equal to -1 and, thus, the dimensionless total flow rate indeed is equal to 1. The closed streamline, which can be seen directly above the interface in the region occupied by water, is symmetrically located around the wave trough. It is generated because of the counterflow of the two fluids, which is also verified by the velocity vectors in the same figure showing oil and water flowing in opposite directions. More specifically, fluid particles in the region occupied by the core fluid, i.e. below the interface, are flowing from left to right, while fluid particles in the region above the closed streamline are flowing in the opposite direction. Very close to the interface, particles of the annular fluid are sheared by the core fluid, whereas, away from it, they are forced to change flow direction owing to the effect of gravity, which points to the left. Thus, this mixed flow of water is caused by the adverse action of gravity, which forces the annular fluid, the heavier of the two fluids, to flow in the direction opposite to that of the core fluid. The steady interface shape, which is composed of only one crest and varies between the radial positions 0.605 and 0.828, exhibits a pronounced maximum to the left of the maximum tube radius (at the mid-plane). This asymmetry is not caused by fluid inertia, which is small here, since, if that were the case, the crest of the interface should appear to the right of the mid-plane of the tube. Instead, it is caused by gravity, which pulls the water backwards, against the oil flow, displacing in this way the maximum of the interface to the left of the mid-plane of the tube. Had the tube wall been straight and for the same dimensionless parameters, the steady interface would be a straight line positioned at radial distance 0.7438. Apparently, this very small variation (10%) of the solid wall from being straight causes disproportionately larger variation ($\sim 25\%$) of the steady interface from that corresponding to the perfect CAF in a straight tube. To obtain this steady solution requires continuation with a fairly small step in the constriction ratio ($\Delta\alpha \approx 0.025$), while solving the nonlinear algebraic set of equations, arising from the discretization of the governing equations, with the Newton–Raphson method. This observation indicates again that the flow field that corresponds to the perfect CAF in a straight tube is quite different from that in a tube of sinusoidally varying cross section.

Figures 3(*b*)–3(*e*) show four different snapshots of the flow field of the time periodic solution within one temporal period, after the system has reached a stable limit cycle. These interfacial shapes are composed of two crests in contrast to the steady solution, which has only one. The fact that the time-dependent interface attains a more wavy form and its variation is larger compared to the steady solution results in the enhancement of the transportation of water inside the troughs of the interface, in

the flow direction of the oil. This, in turn, results in the deceleration of the oil and thus, the oil flow rate is decreased, a conclusion that is in line with the already presented results in conjunction with figure 2. The instantaneous axially averaged core flow rates are found to be $\langle Q_1 \rangle = 3.313$, 3.454, 3.130 and 3.301, respectively, whereas Q_1 attains its maximum, an intermediate, its minimum and again an intermediate value at times corresponding to figures 3(*b*)–3(*e*). It is worth noting that when Q_1 attains its maximum (minimum) value, figure 3(*b*) (3*d*), a crest (trough) of the interface enters the tube. An important observation is that although the closed streamlines in figure 3(*a*) are located in the region occupied by the water adjacent to the troughs of the interface, this does not hold in figures 3(*b*)–3(*e*), as here they are always located at its crests. Apparently, the crests of the interface are now capable of dragging less water in the flow direction of the oil than its troughs in contrast to the steady solution, where crests and troughs drag equal amounts of water. This conclusion is also in line with the observation that whenever a crest of the interface enters the tube, Q_1 is maximized and when a trough of the interface enters the tube, the opposite happens. In figures 3(*b*)–3(*e*), it can be seen that large (small) annular (core) velocities occur above (below) the crests of the interface and by comparing figures 3(*b*), 3(*c*) and 3(*e*) we conclude that the larger the amplitude of the interface the smaller the velocity of the crest. For this reason the left-hand crest in figures 3(*b*)–3(*d*) is drifting faster than the right-hand crest and, thus, the two crests appear to approach each other. On the other hand, when the right-hand crest is forced to decrease its amplitude owing to the tube constriction it accelerates and, thus, the distance between the two crests increases again. This out-of-phase sequence, which is repeated periodically in time, gives rise to a periodic attraction and repulsion of the two crests in space. Furthermore, figures 3(*b*)–3(*e*) show that the closed streamlines at the crests of the interface do not interact strongly with the open ones above them since the Reynolds number is very small ($Re = 0.01 \ll 1$). As the crests of the interface are convected downstream, the closed streamlines around the crests push the open streamlines above them towards the solid wall, thus increasing the water velocity. At axial distances where the troughs of the interface are located, the open streamlines bend downward, their distance increases and the water velocity decreases.

Clearly, there is a great difference between this type of wave and the 'bamboo' waves reported by Li & Renardy (1999) and Kouris & Tsamopoulos (2001*b*), as the latter appear to be steady or nearly steady for an observer moving with the wave velocity. This is not the case here, as the presence of the undulating solid wall forces the wave to deform as it travels downstream and thus, its wave speed changes in time. It is worth noting that Kouris & Tsamopoulos (2002) have shown that the viscosity contrast of the two fluids is responsible for modifying the speed of the bifurcating waves compared to that of the undisturbed interface. More specifically, they have reported that, when the more viscous fluid is centrally located, the wave speed of the saturated travelling wave is always less than that of the undisturbed interface. In order to examine whether this holds in the case of the CAF in a constricted tube, we compute the axially averaged interfacial velocities, denoted as $\langle u_i \rangle$, for both the steady solution, figure 3(*a*), as well as for the solution shown in figures 3(*b*)–3(*e*). These velocities are found to be equal to 21.144, figure 3(*a*); 13.422, figure 3(*b*); 14.062, figure 3(*c*); 13.381, figure 3(*d*) and 13.597, figure 3(*e*). The comparison of these velocities reveals that indeed the saturated wave travels with a time-dependent velocity and this velocity is always much smaller than that of the steady solution, in accordance to what has been observed in the case of the CAF in a straight tube.

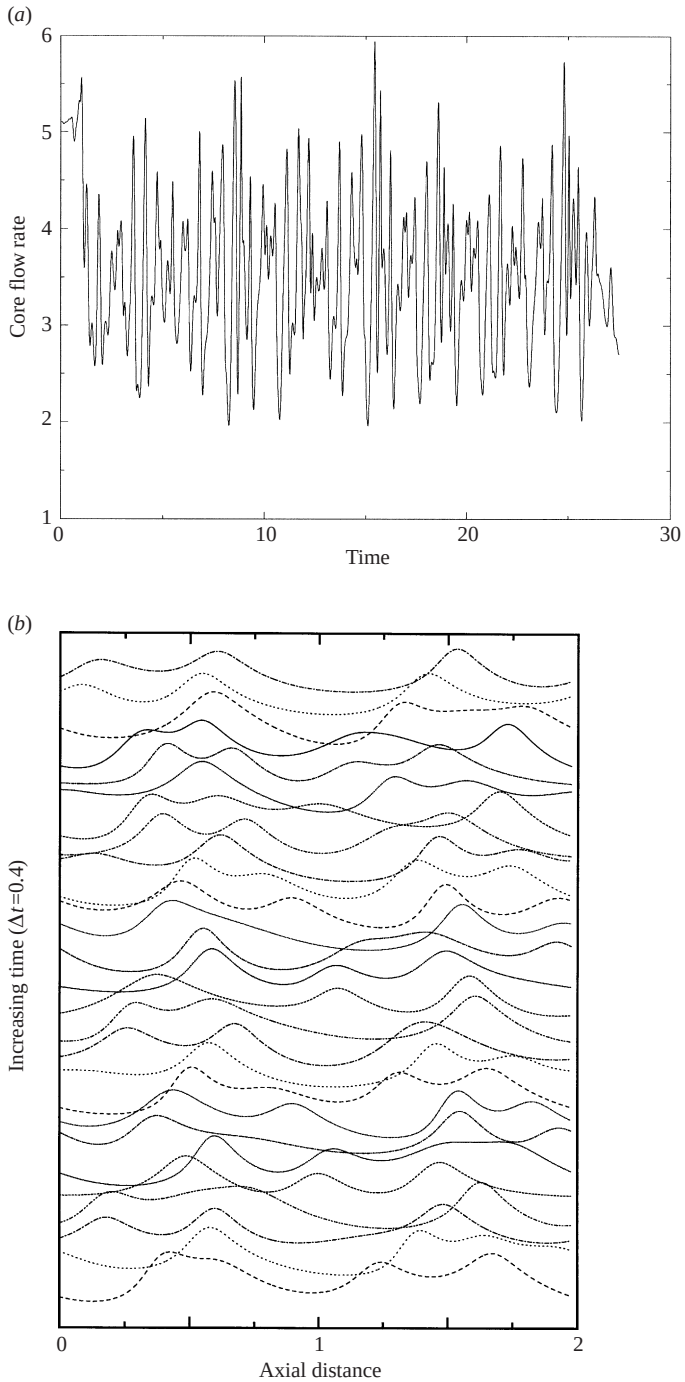

FIGURE 4. (*a*) Time evolution of the core flow rate and (*b*) time evolution of the interface with the first snapshot corresponding to $t = 16.4$ with time steps of 0.4. The time integration has been initiated using the perfect CAF subject to very small and random disturbances $(\alpha, \Lambda, N, V, \mu, \rho, Re, W, F) = (0.9, 1, 2, 0.553, 0.00166, 1.09945, 0.01, 1020, 2389.6)$.

Additionally, we have examined the effect of the length of the domain by increasing the number of unit cells that comprise the undulating tube. More specifically, we have set $N = 2$, instead of 1, doubling the length where periodic boundary conditions are applied, and we have reintegrated the governing partial differential equations. The time integration has been initiated using the steady solution, which is not affected by the increase of N, seeded with the most critical eigenvector corresponding to the above case, $N = 1$. The time evolution of the core flow rate, the velocity field and the shape of the bifurcating travelling wave remain exactly the same as those presented in figures 2 and 3 and for this reason they are not shown again. Thus, we believe that the solution already presented is indeed physically realizable and independent of the number of unit cells that comprise the computational domain.

In addition to increasing the number of the unit cells, we have changed the way that we initialize our time-dependent calculations. More specifically, employing the above-mentioned values of the dimensionless numbers and $N = 2$ we have repeated our calculations using as initial condition the steady solution seeded with random disturbances of very small amplitude. The time evolution of the core flow rate for this case is shown in figure 4(*a*). Clearly, the time evolution of the core flow rate does not follow a pattern, in contrast to what was presented in relation to figure 2. Although at $t = 0$ the flow rate is the same as that corresponding to figure 2, it takes the same short incubation period to deviate from that value and exhibit chaotic behaviour, $t > 1$, varying between the values 1.95 and 5.92, with $\{Q_1\} = 3.46$. Comparing the values of $\{Q_1\}$ that correspond to the different types of initial condition (3.28 and 3.46) that we have used, we conclude that these values deviate by only 5%.

The time evolution of the interface can also be seen in figure 4(*b*) where the first snapshot corresponds to $t = 16.4$ whereas the time difference between successive ones is $\Delta t = 0.4$. Now that the time integration has been initiated with a different initial condition, the saturated interfacial shape is completely different in terms of the number of crests that the wave is composed of. The number of crests of the interface change unpredictably, since for small times the interface is composed of only 2 crests whereas at later times it varies between 2 and 4. On the other hand, the amplitude of this wave is fairly similar to that shown in figures 3(*b*)–3(*e*). By plotting snapshots of the streamlines (Kouris 2000) it can be seen that, for the most part, in the core fluid they smoothly follow the fluid/fluid interface, whereas closed streamlines arise above both the troughs and the crests of the interface in the annular fluid. This strong effect of the initial condition on the dynamics of the saturated travelling wave is not totally unexpected. Frenkel *et al.* (1987), Kawahara (1983), Papageorgiou *et al.* (1990) and Kerchman (1995) have examined the nonlinear dynamics of CAF in a straight tube with the less viscous fluid centrally located and have found similar behaviour. More specifically, Kouris & Tsamopoulos (2002) have found that when the steady solution was seeded with the most unstable eigenvector, a steadily travelling wave resulted, whereas, when the steady solution was disturbed randomly, a chaotic solution was obtained.

3.2. *Core fluid with intermediate Reynolds number* ($Re = 0.1$, *case 2*)

The result of case 1, namely that the inception of nonlinear travelling waves allows them to drag more water inside their troughs decreasing in this way the oil flow rate in comparison to the steady solution, leads us to investigate whether counterflow of two fluids may occur in the linear regime and concurrent flow in the nonlinear one. In order to achieve this, the effect of gravity should be decreased and, for the same pair of fluids, i.e. constant Ga, the Reynolds number must be increased. Figures 5

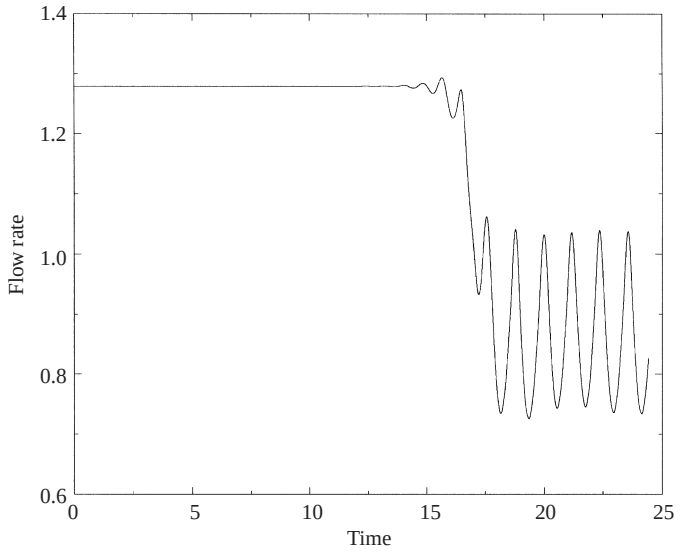

FIGURE 5. Time evolution of the core flow rate
$(\alpha, \Lambda, N, V, \mu, \rho, Re, W, F) = (0.9, 1, 1, 0.553, 0.00166, 1.09945, 0.1, 10.2, 23.9)$.

and 6 (case 2) show the time evolution of the core flow rate for the same values of the dimensionless numbers as in case 1, except for the Reynolds number, which is now equal to 0.1. The core flow rate that corresponds to the steady solution is equal to 1.279, and that of the annular fluid is -0.279, which are very different from those corresponding to case 1 (5.098 and -4.098, respectively). This result should be expected, since the increase in Re decreases F and thus, the force that induces backflow of the water decreases too. Linear stability indicates that this steady solution is unstable and the unstable eigenvalues are reported in table 1. Figure 5 shows that after $t = 15$ the instability of the steady solution becomes visible and at later times, $t > 18$, it is saturated and the system reaches an oscillatory state. The core flow rate, after saturation of the instability, varies between the values of 0.736 and 1.039, with $\{Q_1\} = 0.85$ and that of the annular fluid $1 - \{Q_1\} = 0.15$. Thus, although counterflow of the two phases occurs in the linear regime, concurrent flow does take place in the nonlinear one. The temporal oscillation frequencies in the linear and the nonlinear regimes equal 7.593 and 5.261, respectively. Comparing these frequencies with the linear stability results (table 1) reveals that linear theory is again inadequate to predict the nonlinear frequencies, despite the fact that there is good agreement with the computed frequency obtained by integrating the dynamic equations for small times. The agreement of the frequency of the most unstable eigenmode (eigenvalue 2 in table 1) to the graphically computed one in addition to the fact that the nonlinear shape of the interface is mainly composed of two humps, in accordance with the eigenvector for the interface of the most critical mode, lead to the conclusion that the most unstable mode is indeed excited. It is worth noting that we should not expect exact replication of the linear frequencies even when the system is very close to the steady solution because we do not seed the initial condition with any unstable mode. As a result, we do not control which mode will be excited and a possible excitation of more than one unstable mode cannot be excluded, especially when the growth rates of the unstable modes are quite close to each other, as in this case.

Figure 6(a) shows the streamlines as well as the interface of the computed steady solution. This steady interface has changed considerably compared to the steady

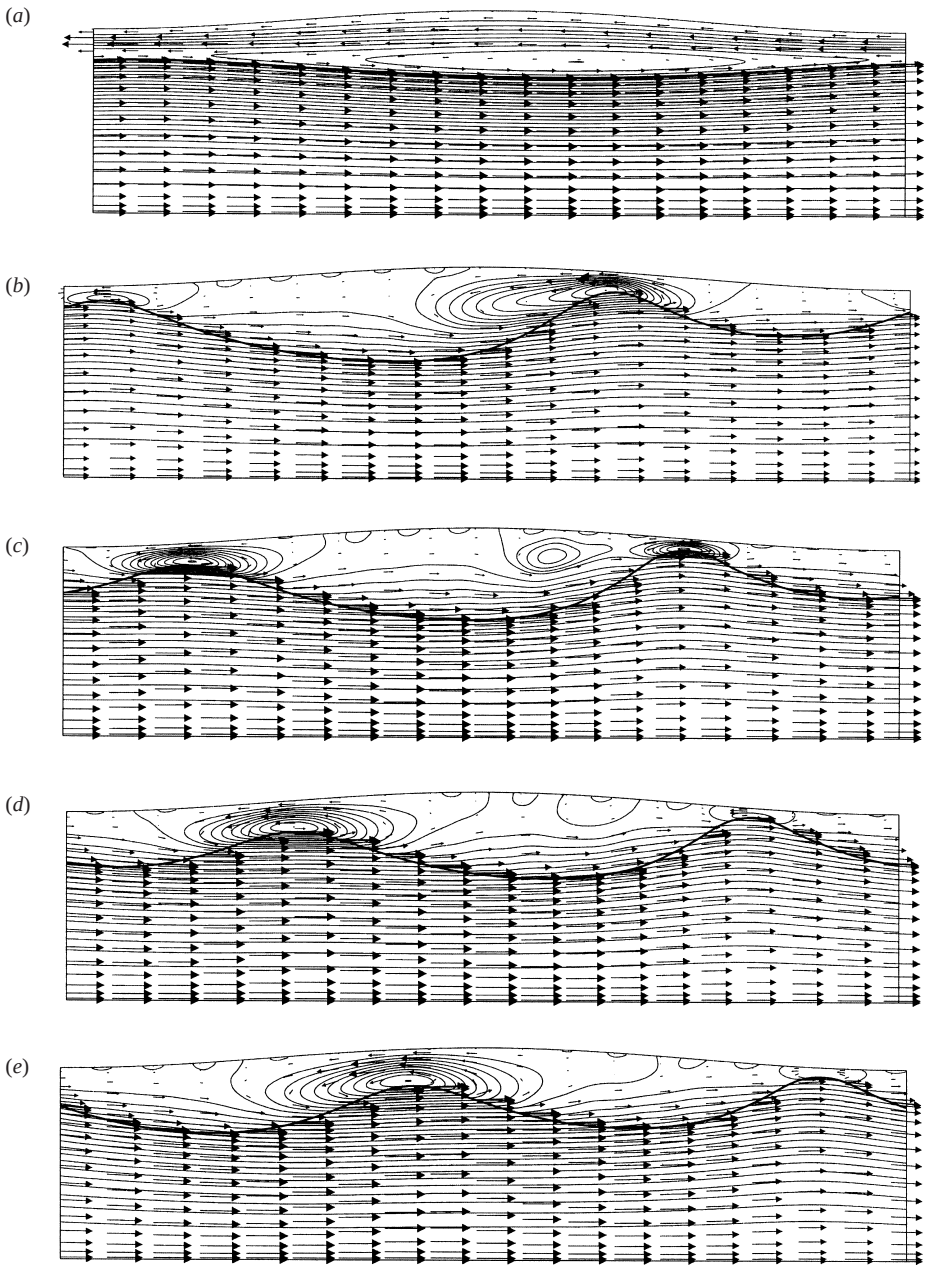

FIGURE 6. Flow fields that correspond to (*a*) the steady solution, (*b*) $t = 22.4825$, (*c*) $t = 22.7325$, (*d*) $t = 22.9825$, (*e*) $t = 23.2325$ $(\alpha, \Lambda, N, V, \mu, \rho, Re, W, F) = (0.9, 1, 1, 0.553, 0.00166, 1.09945, 0.1, 10.2, 23.9)$.

shape shown in figure 3(*a*) since its maxima and minima are less pronounced. The interface varies between the values 0.671 and 0.750 and it appears to have a minimum to the right of the tube maximum (the mid-plane). Although there are again closed streamlines located directly above the interface, these occupy a larger portion of annular fluid domain, leaving a much smaller region for the water to flow backwards in the direction of gravity in contrast to case 1. It is also worth noting that even

in this case the closed streamlines are located at the troughs of the steady interface, similar to figure 3(*a*). The comparison of the axially averaged interfacial velocities that correspond to the steady solutions of cases 1 and 2 shows that increasing *Re* by an order of magnitude causes a drastic decrease in $\langle u_i \rangle$ as this is equal to 5.104 here, whereas in case 1 it is equal to 21.144. This trend is easily explained, since increasing *Re* from 0.01 to 0.1, decreases both *F* from 2389.6 to 23.9 and the volumetric flow rate of the oil from 5.098 to 1.279 and thus, the axially averaged interfacial velocity.

Snapshots of the interfacial shapes as well as the associated streamlines at different times can be seen in figures 6(*b*)–6(*e*). In line with figures 3(*b*)–3(*e*), we can see that the interfacial shapes are not steady even for an observer moving with the interface. Furthermore, the amplitude of the saturated travelling wave is smaller than the previous case, i.e. increasing *Re* reduces the saturation amplitude of the travelling wave, still, the wave exhibits more pronounced maxima and minima compared to the steady solution (figure 6*a*). The interface is mainly composed of two humps and when they enter the expanding portion of the tube, they decelerate and increase their amplitudes, whereas upon entering the contracting portion of the tube, they accelerate and decrease their amplitudes. This phenomenon produces waves that repel and attract each other periodically without ever colliding. The instantaneous axially averaged core flow rates are equal to 0.865, 0.821, 0.854 and 0.897, respectively, whereas the corresponding values of the axially averaged interfacial velocities are 3.500, 3.311, 3.426 and 3.596, respectively. The difference between figures 3(*b*)–3(*e*) and figures 6(*b*)–6(*e*) is that in the latter there are open streamlines located below the closed ones, which run along the annular fluid domain in contrast to case 1, since here we deal with concurrent flow of both fluids. In these figures, it can also be seen that each crest of the interface is encircled by a streamline with a zero value streamfunction, since it ends at the solid wall. Moreover, the intensity of the vortex increases in the expanding portion of the tube and diminishes in the contracting one. These vortices force the open streamlines in the water to bend downwards, cross the interface and enter the core flow region, whereas far from them they bend upwards and enter the annular region again. Note here that in the sequence of figures 6(*b*)–6(*e*), small vortices with streamlines intersecting the tube wall appear and disappear periodically. In the sequence of figures 6(*b*) and 6(*c*), we also observe that the large vortex that encircles the right-hand crest in figure 6(*b*), evolves into two smaller ones, which are both located inside a loop ending at the wall, as the crest of the interface approaches the solid surface. In figure 6(*d*), the previous two small vortices are completely disintegrated and then they are absorbed by the vortex that is located above the oncoming crest (figure 6*e*). Furthermore, the velocity of the interface at its crests appears to be smaller than the values at its troughs. Thus, the larger the amplitude of the wave, the steeper the wave becomes, which is consistent with the Kuramoto–Shivashinsky wave steepening predictions. Possibly then, if we increase the Reynolds number further, the waves may break up forming small drops of the core fluid inside the annular one.

3.3. *Core fluid with large Reynolds number* ($Re = 0.25$, *case 3*)

Figures 7 and 8 (case 3) correspond to an even larger value of the Reynolds number ($Re = 0.25$) than the previous two cases. The time evolution of the core flow rate for this case is given in figure 7. It can be seen that the core flow rate, which initially is equal to 0.985, departs from the steady solution executing oscillations of frequency 6.46, which compares favourably with the computed linear temporal frequency (eigenvalue 2 in table 1). After $t = 15$, the core flow rate reaches an

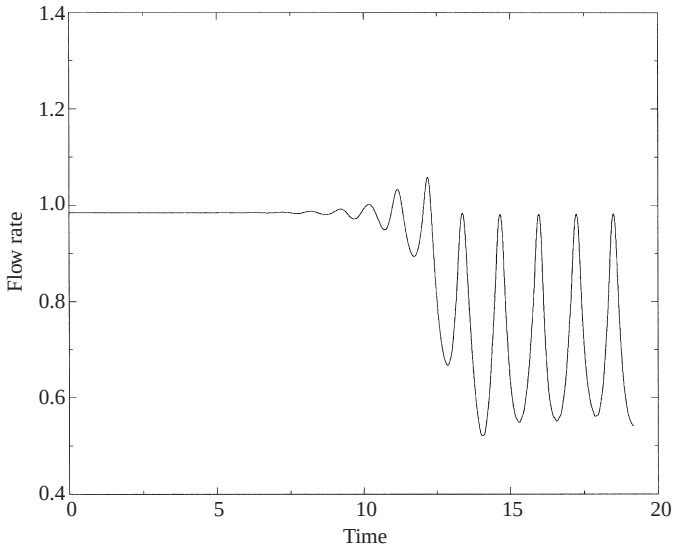

FIGURE 7. Time evolution of the core flow rate
$(\alpha, \Lambda, N, V, \mu, \rho, Re, W, F) = (0.9, 1, 1, 0.553, 0.00166, 1.09945, 0.25, 1.632, 3.823)$.

oscillatory state of constant amplitude between the values 0.55 and 0.98 of frequency approximately 4.85, while its time averaged value equals $\{Q_1\} = 0.7$. Although for this value of the Reynolds number concurrent flow of the two phases occurs in both the linear and the nonlinear regime, the solution after saturation of the instability is associated again with a lower average volumetric flow rate of the oil than the steady value ($0.7 < 0.985$). The streamlines as well as the interface corresponding to the steady solution are given in figure 8(a), where it can be seen that there are open streamlines both below and above the closed streamlines in the region occupied by water. The open streamlines on top indicate that water exits the tube from its left-hand side resulting in this way in a negative volumetric flow rate, whereas open streamlines next to the interface result in a positive water flow rate. Their net effect on the flow of the water is that water is flowing from left to right, since its flow rate computed using figure 7 ($t = 0$) is small but positive; it is equal to 0.015. The steady interface is virtually straight as it varies between the values 0.69 and 0.72, figure 8(a), whereas the time periodic interface is composed again of two crests per unit cell and varies between the values 0.604 and 0.882 at $t = 19.15$.

Snapshots of the flow field of the two phases corresponding to the time periodic solution are shown in figures 8(b)–8(e). The instantaneous axially averaged core flow rates at these time instances are found to be $\langle Q_1 \rangle = 0.71$, 0.716, 0.71 and 0.70, respectively. In these four figures we can see that the closed streamlines are above the open ones close to the solid wall, in contrast to figures 3(b)–3(e). Comparing the averaged values of the core flow rate within one temporal period for the three different values of the Reynolds numbers (cases 1–3) it appears that the larger the Reynolds number, the smaller the variation of the core flow rate is. More specifically, the variation of the core flow rate in the three examined cases is 10%, 9% and 2%, respectively. Keeping in mind that in a straight tube the 'bamboo' waves were travelling with a constant wave speed without being deformed and, thus, the averaged core flow rate was constant in time in addition to the fact that the constriction ratio here is close to 1, the decreasing variation of the core flow rate with increasing Re

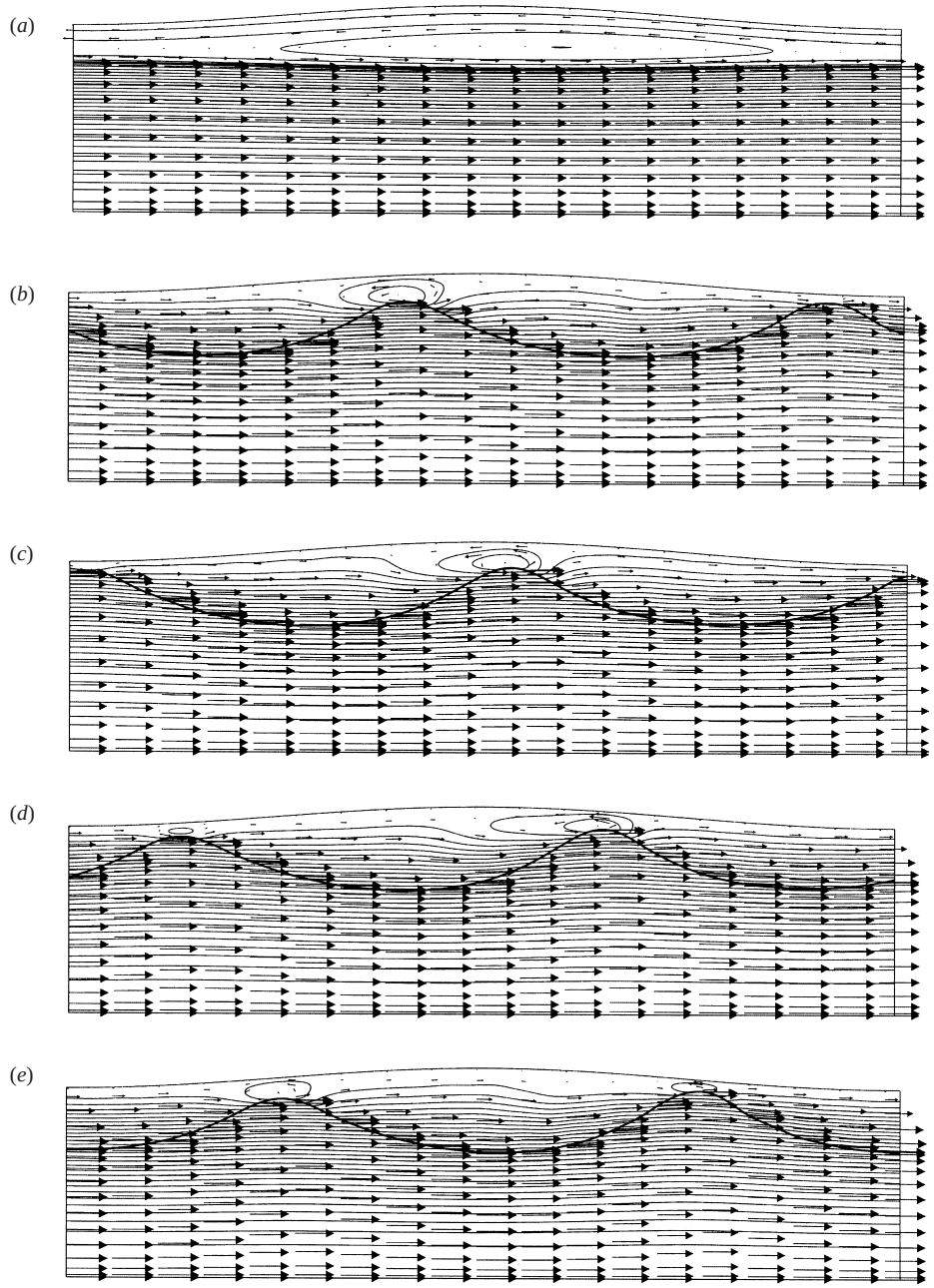

FIGURE 8. Flow fields that correspond to (*a*) the steady solution, (*b*) $t = 18.25$, (*c*) $t = 18.55$, (*d*) $t = 18.85$, (*e*) $t = 19.15$ $(\alpha, \Lambda, N, V, \mu, \rho, Re, W, F) = (0.9, 1, 1, 0.553, 0.00166, 1.09945, 0.25, 1.632, 3.823)$.

indicates a tendency towards the limit of waves of constant wave speed similar to what has been observed in a straight tube (Li & Renardy 1999; Kouris & Tsamopoulos 2002). This conclusion is also in accordance with the computed mean interfacial velocities of the saturated solution. More specifically, the amplitude of the variation of the velocities in case 1, 2 and 3 is 0.3405, 0.1425 and 0.0315, respectively. Comparing

now the amplitude of the time-dependent solutions shown in figures 3, 6 and 8, we conclude that increasing *Re* indeed reduces the amplitude of the bifurcating travelling wave.

4. Moderate constriction ratio ($\alpha = 0.8$): effect of μ, W and F

Figure 9 (case 4) presents the time evolution of CAF for the following values of the dimensionless numbers $(\alpha, \Lambda, N, \mu, \rho, J, Ga, V, Re) = (0.8, 1, 1, 0.00166, 1.09945, 0.102, 2.4028, 0.552, 0.1)$. These dimensionless numbers are the same as those of case 2 except for the constriction ratio, which here is equal to 0.8, instead of 0.9. This case requires a long incubation period for instability to arise. The exponential deviation in a Q_1 *vs.* time plot becomes visible only for $t > 25$, whereas for $t > 40$ the flow approaches an oscillatory state of constant amplitude (see Kouris 2000). At $t = 0$, the steady core flow rate is equal to 0.965, whereas after saturation of the instability, it varies between the values $Q_1 = 0.763$ and 0.989. Comparing the steady water flow rates that correspond to cases 2 and 4 (-0.279 and 0.035, respectively) we conclude that the decrease in the constriction ratio causes water and oil to flow concurrently. This result is easily explained considering the increase in the tube undulation as a way of hindering the flow of water in both directions. However, the shear exerted by the core fluid still drags some of the water along its path and, as a result, the two fluids flow concurrently even at steady state, in contrast to case 2. The temporal oscillation frequency is equal to 6.119 initially and 5.6647 at later times. In particular, the first of these frequencies correlates well with those computed using the linear theory which are shown in table 2 and more specifically with that corresponding to the most unstable mode (eigenvalue 2). Although the decrease in the constriction ratio causes a qualitative difference in the steady-state solution as explained above, the corresponding averaged oil flow rates of the time periodic solution do not change appreciably since, in case 2, $\{Q_1\} = 0.85$ and, in case 4, $\{Q_1\} = 0.88$.

Figure 9(*a*) shows the flow field that corresponds to the steady solution. The steady interface is composed of a single crest per unit cell and varies between the values 0.604 and 0.755 at axial locations of 0.517 and 0.023, respectively, in a cell of total length 1. Comparison of the steady shape with that corresponding to case 2 reveals that although both shapes exhibit a minimum at the mid-plane of the tube and a maximum at its neck, the decrease in the constriction ratio causes greater variations of the steady interface. The closed streamlines are located in the expanding portion of the tube and there is no open streamline above them. This verifies the conclusion that concurrent flow of both phases occurs. The axial mean interfacial velocity of the steady solution is found to be $\langle u_i \rangle = 4.384$.

Figures 9(*b*)–9(*e*) show four snapshots of the flow field that correspond to the time periodic solution, within one temporal period. The computed values of the spatially mean core flow rates are $\langle Q_1 \rangle = 0.800$, 0.896, 0.955 and 0.8369, whereas the values of the axially averaged interfacial velocities are $\langle u_i \rangle = 3.602$, 3.994, 4.267 and 3.795. The characteristic of these figures, in accordance with the previous results, is that there are two wave crests per unit cell and several vortices of varying strength, which coexist one inside the other. As the interface travels downstream, new vortices are created, while others either diminish in intensity or even disappear and reappear periodically. Of course, these observations are not entirely unexpected, since water flows in the annulus with viscosity 600 times smaller than that of the oil and values of the *Re* are based on oil properties. As a result, the Reynolds number based on the properties of the water is at least 2 orders of magnitude greater than that we report based on

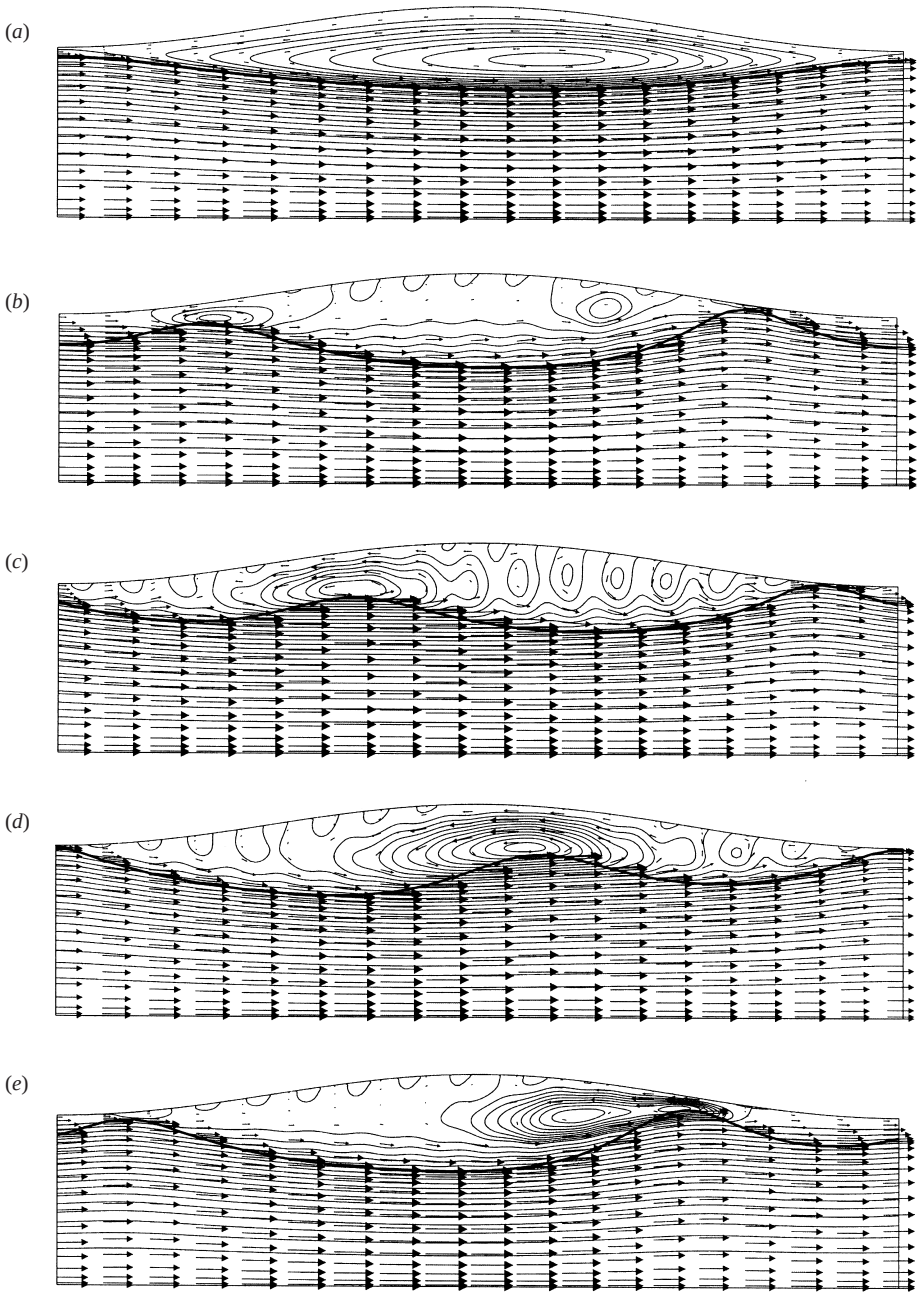

FIGURE 9. Flow fields that correspond to (*a*) the steady solution, (*b*) $t = 43.05$, (*c*) $t = 43.35$, (*d*) $t = 43.65$, (*e*) $t = 43.95$ $(\alpha, \Lambda, N, V, \mu, \rho, Re, W, F) = (0.8, 1, 1, 0.552, 0.00166, 1.09945, 0.1, 10.2, 23.9)$.

the properties of the oil. It is also interesting that as the interface approaches the solid wall, especially at axial distances where the radius of the solid wall attains its minimum value, the region between the free surface and the wall becomes very thin and no recirculation of water is observed, see the interface maximum in the right-hand side of figures 9(*b*)–9(*d*). In the case of the straight tube geometry, Li & Renardy (1999) and Kouris & Tsamopoulos (2001*b*) have shown that the 'bamboo' waves are

	Unstable eigenvalues			
Number	Case 4	Case 5	Case 6	Case 7
1	0.2340 ± 1.653i	0.9203 ± 2.945i	0.7718 ± 2.430i	3.993 ± 1.761i
2	0.3708 ± 6.108i	—	0.4414 ± 2.494i	—
3	0.0458 ± 10.79i	—	0.4368 ± 27.92i	—

TABLE 2. Unstable eigenvalues for: $(\alpha, \Lambda, N, \rho, V, Re, W) = (0.8, 1, 1, 1.09945, 0.552, 0.1, 10.2)$; and case 4: $\mu = 0.00166$, $F = 23.9$, $W = 10.2$; case 5: $\mu = 0.00166$, $F = 23.9$, $W = 102$; case 6: $\mu = 0.00166$, $F = -23.9$, $W = 10.2$; case 7: $\mu = 0.0166$, $F = 23.9$, $W = 10.2$.

closely associated with the presence of small vortices directly above the crests of the interface which travel downstream with the same speed as the interface. This is not the case here as the axial variation of the radius of the solid wall causes the creation of many small vortices not only above the crests of the interface, but also above its troughs, whereas some of them form and disappear periodically in time. Comparing now the mean interfacial velocities $\langle u_i \rangle$ between cases 2 and 4, we conclude that decreasing α decreases $\langle u_i \rangle$ of the steady solution and increases the variation of $\langle u_i \rangle$. Indeed, in case 2, $\langle u_i \rangle$ varies between 3.311 and 3.596, whereas in case 4, $\langle u_i \rangle$ varies between 3.602 and 4.267.

4.1. *Effect of the Weber number (case 5), mechanisms leading to discontinuous flow of the core fluid*

In order to examine the effect of surface tension, we have simulated the core–annular flow that corresponds to the same values of the dimensionless numbers as in case 4 except for the inverse Weber number, which is increased by an order of magnitude, i.e. to $W = 102$, instead of 10.2. Table 2 indicates that only one unstable eigenvalue exists now (case 5). The transition from the steady solution to the time periodic solution causes the core flow rate, which is initially equal to 0.975, to vary rather irregularly and between the values 0.69 and 0.99, with $\{Q_1\} = 0.89$ (Kouris 2000). The comparison of these values with those of case 4 makes apparent that the increase in W by an order of magnitude does not change the core flow rate of either the steady or the time periodic solution significantly. The fact that the amplitude of the variation of the core flow rate is much greater than that of case 4 is due to the fact that here interfacial waves of greater amplitude develop.

This is verified in figure 10, where the steady interface as well as snapshots of the interface after achieving a quasi-periodic flow can be seen. Also, without doubt, the saturation amplitude of the bifurcating travelling waves is an increasing function of the surface tension parameter W, a result which is in accordance with previous analyses, see Kerchman (1995) and Kouris & Tsamopoulos (2002). In the latter study (with $\mu > 1$), it has been shown that the increase of the surface tension, apart from reducing significantly the speed of the travelling wave compared to the undisturbed interfacial velocity, promotes the creation of lobes which are connected with virtually flat segments of the interface. This is in qualitative agreement with the experiments performed by Aul & Olbricht (1990). Of course, those wave shapes do not resemble at all those shown in figures 10(*b*)–10(*e*), which are greatly modified by the periodically varying solid wall, although they retain a 'sawtooth' like shape. As far as the steady interface is concerned, it varies between the values 0.612 and 0.742 and comparing these values with those for the steady solution shown in figure 9(*a*), we conclude that

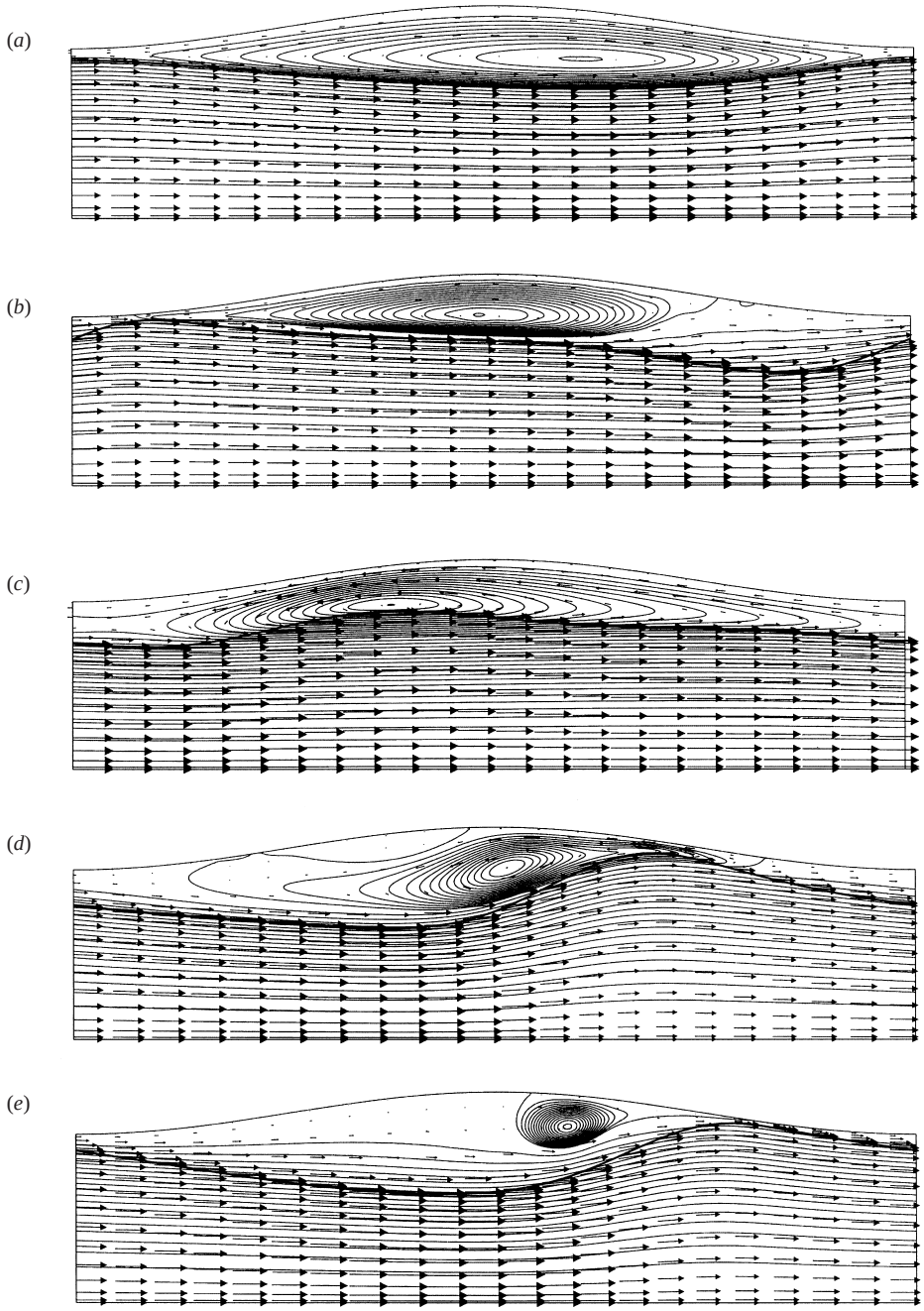

FIGURE 10. Flow fields that correspond to (*a*) the steady solution, (*b*) $t = 42.25$, (*c*) $t = 42.75$, (*d*) $t = 43.25$, (*e*) $t = 43.75$ $(\alpha, \Lambda, N, V, \mu, \rho, Re, W, F) = (0.8, 1, 1, 0.552, 0.00166, 1.09945, 0.1, 102, 23.9)$.

increasing W instead of increasing the amplitude of the steady interface, it decreases it, which is a direct result of the increased capillary force trying to diminish steady interfacial waves.

Figure 10(*a*) shows the steady solution with which the time integration has been initiated. The mean value of the interfacial velocity for this case is found to be

$\langle u_i \rangle = 4.375$. Comparing cases 4 and 5, we conclude that the larger W is, the larger the region, which the closed streamlines occupy in the annular flow domain. For the flow fields that correspond to figures 10(*b*)–10(*e*) the axially averaged core flow rates are found to be $\langle Q_1 \rangle = 0.856$, 1.123, 0.882 and 0.789, whereas the corresponding axially averaged interfacial velocities are equal to $\langle u_i \rangle = 3.857$, 4.971, 4.180 and 3.678; the larger the value of $\langle Q_1 \rangle$ is, the larger the value of $\langle u_i \rangle$ becomes. The sequence of these figures shows that, as the crest of the interface travels downstream, it deforms considerably and, as a result, allows great variations of the flow field inside the tube. Only in figure 10(*c*) is the centre of the vortex located directly above the interface; in all the other figures the centre of the vortex is either to the right (figure 10*b*) or to the left (figures 10*d* and 10*e*) of the crest. Common among these instantaneous flow fields is the existence of only one large vortex inside the tube and, although in figures 10(*b*), 10(*d*) and 10(*e*) this vortex is located in the region occupied by water, this is not the case in figure 10(*c*), where the interface and portion of the oil is encircled by the vortex. The fact that the total flow is kept constant throughout the simulation in addition to the fact that the interface is crossed by the vortex in figure 10(*c*) result in a negative flow rate of the water at that instant. Hence, some of the water exits the tube from its left-hand side. In figure 10(*d*), the wave has become even steeper than that presented in figures 10(*b*)–10(*c*) and at the same time it has increased its amplitude. Further steepening of the wave does not occur; otherwise this would result in the breakup of the wave (see next simulations). Here, the solid wall forces the interface downwards and consequently the crest velocity increases, the crest accelerates and eventually escapes the constriction. Comparing now the interfacial velocities that correspond to cases 4 and 5, we reach the conclusion that the increase in W by an order of magnitude, although it does not affect appreciably $\langle u_i \rangle$ of the steady solution, increases considerably the variation of $\langle u_i \rangle$ of the time periodic solution. This variation in case 5 is between the values 3.678 and 4.971 within one temporal period.

Next, we examine whether the increase of interfacial tension, apart from giving rise to travelling waves of larger amplitude, can promote breakup of the interface and subsequent creation of slugs of core fluid in the continuous stream of the annular fluid. To this end, we increase the coefficient of surface tension five times compared to that of case 5, whereas all other dimensionless numbers are kept the same, i.e. now $W = 510$. The steady solution, which is used as an initial condition, is almost flat with a shallow minimum near the tube maximum and a single large vortex above it (Kouris 2000). Apparently, owing to gravity, water flows against the applied shear from the core fluid, as in previous cases. However, this solution is unstable and figure 11(*a*) shows four different snapshots of the interface taken at time intervals $\Delta t = 0.25$. At $t = 6.2$ and $t = 6.45$, the interface is slightly translated downstream in the axial direction with an increasing amplitude. This is further intensified at $t = 6.7$, while the solid line corresponds to the last time step before breakup of the interface ($t = 6.95$). These snapshots of the interface, apart from showing the time evolution of the interface, indicate that the wave amplitude increases exponentially ($\sim \exp(6.5t)$) with time just before breakup.

In figure 11(*b*), we show to what the flow field evolves just before breakup, at $t = 6.95$. Now, two large vortices are located to the left and right of the minimum of the interface. The left-hand vortex rotates clockwise and pushes core fluid to the left of the minimum of the interface, while the right-hand vortex rotates counterclockwise and pushes fluid to the right of the minimum. The net effect is that just before breakup the core fluid undergoes an extensional flow forming a rather broad minimum, like a

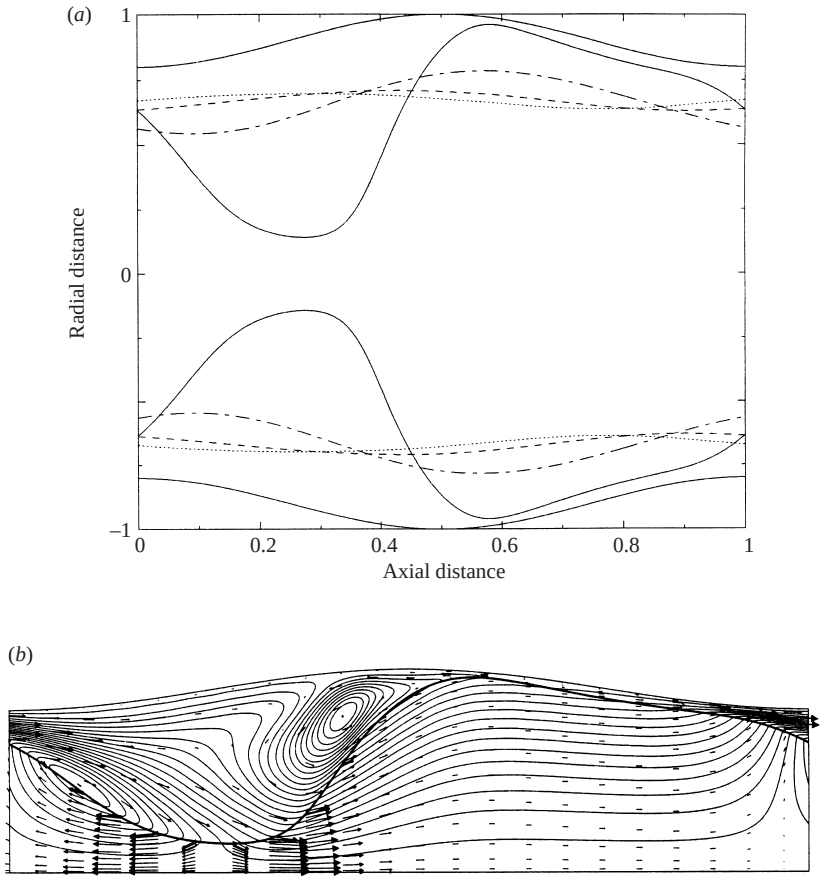

FIGURE 11. (*a*) Interfacial shapes that correspond to ·····, $t = 6.2$, ----, $t = 6.45$, −·−, $t = 6.7$, ——, $t = 6.95$ and flow field that corresponds to (*b*) $t = 6.95$, $(\alpha, \Lambda, N, V, \mu, \rho, Re, W, F) = (0.8, 1, 1, 0.552, 0.00166, 1.09945, 0.1, 510, 23.9)$.

long neck. This neck thins continuously and the interface moves towards the centreline for mass conservation reasons.

A rather different flow type arises just before breakup, when the core fluid is the less viscous of the two. It has been shown in earlier stability analysis (Hickox 1971; Kouris & Tsamopoulos 2001*a*) and dynamic simulations (Kouris & Tsamopoulos 2002) that such flows are more susceptible to instabilities. Thus, they require a thinner annular fluid for even temporary stabilization. In figure 12, we present the time evolution of the CAF for the following values of the dimensionless numbers: $(\alpha, \Lambda, N, \mu, \rho, V, Re, W, F) = (0.8, \frac{1}{4}\pi, 4, 10, 1, 0.826, 0.05, 40\,000, 0)$. These values correspond to a tube consisting of 4 unit cells, the minimum radius of which is 0.8 times its maximum one, while the axial length of each unit cell is 8 times its maximum radius. As a result, the total length of the tube is 32 times its maximum radius. The fluid in the annulus is 10 times more viscous than that in the core, while the fluids have equal densities and, as a result, gravity does not enter the problem. We have assigned a very large value to W in order to promote breakup of the fluid/fluid interface and creation of discontinuous flow of the core fluid similar to the previous case. The time-evolution of the core flow rate, shown in figure 12(*a*), exhibits a much longer incubation period, similar to those observed for CAF in a straight tube with the more

viscous fluid in the annulus (Kouris & Tsamopoulos 2002). Subsequently, there is an exponential deviation from the steady solution, but this instability cannot be saturated. The time evolution of the interface towards breakup is shown in figures 12(*b*) and 12(*c*). Here, a small disturbance is followed as it travels and evolves in the tube. When a trough of the interface enters the expanding portion of the tube, the wave deformation decreases, a crest is slowly formed and, before entering the next tube constriction, a trough reappears, albeit with larger amplitude than it had entering this unit cell. In other words, the tube undulation amplifies the disturbance, but the interface, except for the portion around the wedge, moves slightly. Our computations break down just after $t = 835.98$, and the deformed shape of the interface at that time is shown in figure 12(*c*) (solid line). Now the interface seems to form a narrow wedge, as opposed to a long neck shown in figure 11(*a*). This finger, being now initiated from the more viscous annular fluid and directed towards the less viscous one, accelerates continuously and becomes more pointed as it approaches the axis of symmetry. Figures 12(*b*) and 12(*c*) demonstrate that, as the disturbance is convected downstream, it increases its amplitude but leaves behind the interface almost undisturbed. Therefore, this case is convectively unstable.

Figure 12(*d*) shows the instantaneous streamlines, the interface (thick line) as well as the velocity field at $t = 835.98$. Clearly, there is a great difference between the flow field corresponding to figure 11(*b*) and that to figure 12(*d*). In the former case, the two counter-rotating vortices located before and after the trough are responsible for draining the core fluid and forcing the interface to intersect the centreline, while at the same time, the neighbouring crest of the interface is moving upwards, towards the solid wall. Moreover, the velocity field is equally intense in the core and the annular fluids. In the latter case, the core fluid does not seem to undergo a squeeze flow for as long as computations are possible. The intensity of the flow in the annular region is much smaller than that in the core and as a result the interface is responding to the changes occurring in the flow field of the core and not of the annular fluid. This last observation is in accordance with the dynamic results presented by Kouris & Tsamopoulos (2002) for CAF in a straight tube. In that case, we have changed the inverse Weber number by more than five orders of magnitude, keeping the more viscous fluid in the annulus and observed that the flow field in the annular domain was much less intense than that of the core. However, there the maximum value of W was three times smaller than the present one, but no breakup of the interface was observed.

4.2. *Gravity acts in the flow direction of the core fluid* (*case 6*)

Figures 13 and 14 (Case 6) correspond to the same values of the dimensionless numbers as those of case 4, except that gravity now acts in the same direction as the mean flow of the core fluid, in this way accelerating the water. So we use here $F = -23.9$ as the value of the inverse Froude number, instead of 23.9. In figure 13 we give the time evolution of the core flow rate computed at the entrance of the tube. The steady (and for the dynamic simulations initial) flow of the core fluid is very small, 0.086, because gravity pulls the heavier water in the annulus preferentially downward. There is an abrupt transition of the core flow rate from this initial value for $t > 30$, whereas the new oscillatory state is characterized by a continuous variation of the core flow rate between the values 0.111 and about 0.6, with $\{Q_1\} = 0.27$. The difference between this figure and the previous ones is that now nonlinearity leads to considerable acceleration of the core and, consequently, deceleration of the water. More specifically, the mean core velocity in the nonlinear regime is increased by more

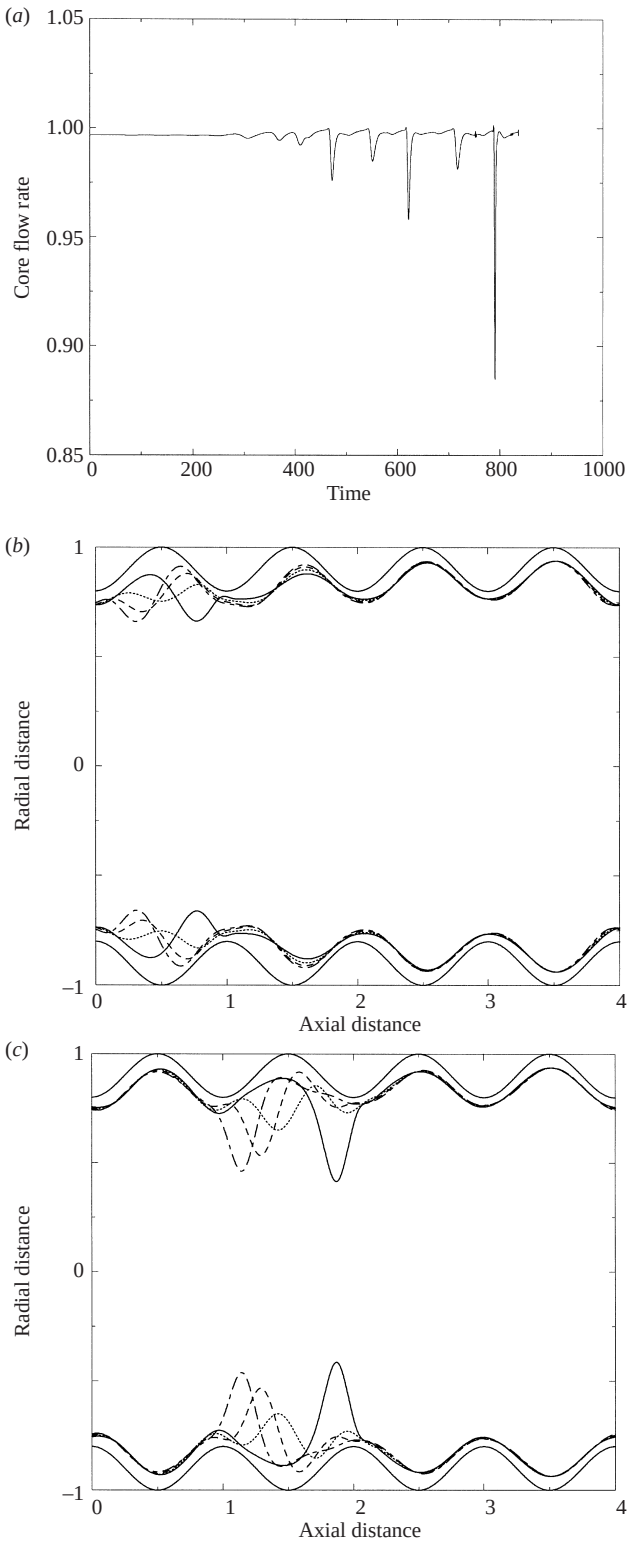

FIGURE 12(*a–c*). For caption see facing page.

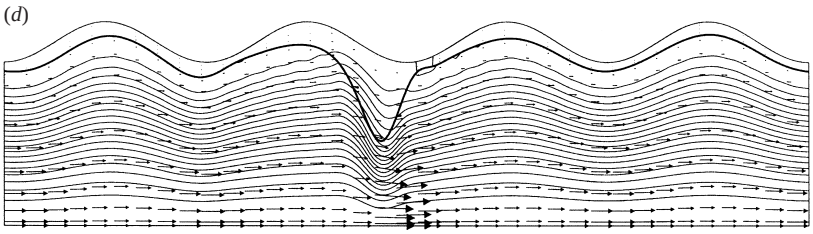

FIGURE 12. (*a*) Time evolution of the core flow rate, instantaneous shapes of the interface for (*b*) –·–, $t = 806.33$, ----, $t = 810.33$, ·····, $t = 814.33$, ——, $t = 818.33$, (*c*) –·–, $t = 823.78$, ----, $t = 827.78$, ·····, $t = 831.78$, ——, $t = 835.78$, (*d*) the flow field corresponding to $t = 835.98$ $(\alpha, \Lambda, N, V, \mu, \rho, Re, W, F) = (0.8, \frac{1}{4}\pi, 4, 0.826, 10, 1, 0.05, 40\,000, 0)$.

than 310% compared to the value that corresponds to the steady state. The computed frequency of the oscillation using figure 13 is found to be 2.668 in the linear regime and 3.191 in the nonlinear regime. In other words, the linear frequency is within the frequencies of the unstable modes predicted by the linear theory, as reported in table 2.

The steady solution presented in figure 14(*a*) appears to be very regular, as no backflow or recirculation of water takes place while the steady interface varies between the values 0.561 and 0.775. The velocity of the less viscous and heavier annular fluid is much larger than that of the core fluid and neither varies considerably along the tube. In the scale of this figure, the oil in the core seems to have an almost uniform (and zero) velocity in each cross-section compared to the velocity of the water, which has a parabolic profile in the radial direction. The interface (thick line) smoothly follows the tube wall, and its maxima and minima almost coincide with those of the tube wall. This is different from the situation in figure 9(*a*), in which the interface maxima almost coincide with the tube minima and vice versa, because there gravity acts against the flow of the core fluid and forces the heavier annular fluid in the opposite direction to the core flow. Thus, the water flow rate in the former case is much smaller than in the latter, and for that reason there is a great difference between the core flow rates of the steady solution, see figure 13 ($0.086 \ll 0.965$). Furthermore, the position of the crest of the steady interface is directly responsible for the appearance of the closed streamlines in the annular flow domain, see figure 9(*a*), in contrast to the flow field shown in figure 14(*a*), where no closed streamlines exist. For the same reason, the mean interfacial velocities of the steady solutions of cases 4 and 6 deviate so much from each other, as in case 4 it is equal to 4.384 and in case 6 it is equal to 0.437.

Figures 14(*b*)–14(*e*) show the flow field as well as the interface at different times after saturation of the instability. For these snapshots of the flow field, the corresponding values of the spatially mean core flow rates are $\langle Q_1 \rangle = 0.308$, 0.316, 0.226 and 0.219, while the instantaneous axially averaged interfacial velocities are $\langle u_i \rangle = 1.387$, 1.399, 0.992 and 0.972, respectively. In all figures 14(*b*)–14(*e*), we observe that there is a great difference of the intensity of the flow between the more viscous oil and the water, and both vary along the tube in contrast to the steady flow (figure 14*a*). The core fluid is flowing primarily due to shear exerted by the water. This conclusion is in line with the observation that larger oil velocities are observed, not where the oil flow cross-section is minimized, but where larger velocities arise in the annular film. For mass conservation reasons, this occurs where the cross-section in the annular region is minimized, i.e. around the maxima of the interface in figures 14(*b*)–14(*e*). The strong effect of gravity on the dynamics of the CAF becomes evident by comparing the

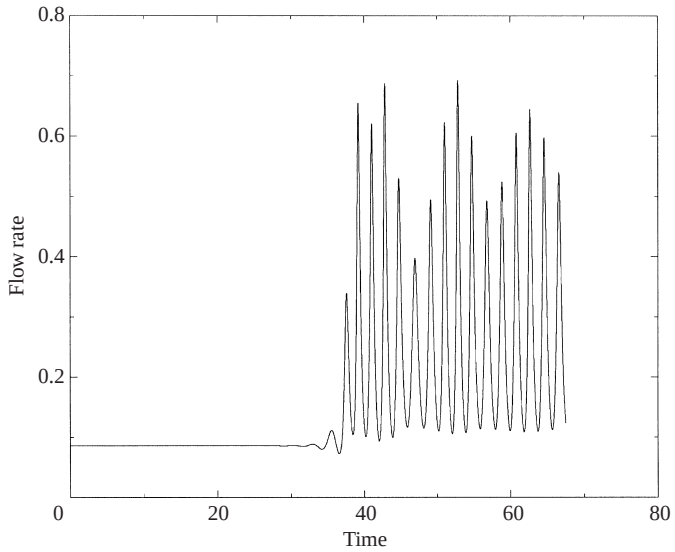

FIGURE 13. Time evolution of the core flow rate
$(\alpha, \Lambda, N, V, \mu, \rho, Re, W, F) = (0.8, 1, 1, 0.552, 0.00166, 1.09945, 0.1, 10.2, -23.9)$.

corresponding values of $\langle u_i \rangle$ of cases 4 and 6. In the former case, gravity decreases further the interfacial velocity compared to that of the steady solution, whereas in the latter the opposite occurs.

4.3. *Effect of viscosity ratio, μ (case 7)*

In order to examine the effect of the viscosity ratio, we have increased its value compared to that of case 4 by an order of magnitude, i.e. to $\mu = 0.0166$ (case 7), instead of 0.00166. The core flow rate at the entrance of the tube, after an incubation period ($0 < t < 300$), attains an oscillatory state of frequency 1.841 in the linear and 1.683 in the nonlinear regime. The core flow rate that corresponds to the steady solution is equal to 0.796, whereas it varies in the nonlinear regime between the values 0.693 and 0.905, with $\{Q_1\} = 0.777$. Comparing the values of the core flow rate of the steady solution with that of the time periodic solution, we conclude again that the nonlinear regime is associated with a small deceleration of the core fluid, which is approximately 2%, in contrast to case 4, where it is 9%. Linear theory reveals that the steady solution is unstable with only one unstable mode (table 2), whereas the frequency computed using linear stability theory is exactly the same as that integrating in time the governing equations for small times. Figure 15(*a*) shows the steady flow with a single vortex located in the mid-plane of the tube. The axially mean interfacial velocity for this case is equal to $\langle u_i \rangle = 3.469$. The steady shape of the interface is slightly curved pointing towards the expansion, whereas the core velocity field approaches that of plug flow. The increase of the viscosity ratio by an order of magnitude relocates the maximum of the steady interface (compare figures 9*a* and 15*a*), in a similar way with the change in the direction of gravity, case 6. Using the same arguments as in case 6, the decrease of the steady core flow rate and the deviation of the undisturbed interfacial velocities of cases 4 and 7 with increasing the viscosity ratio are easily explained.

Figures 15(*b*)–15(*e*) show the flow field within one temporal period after complete saturation of the instability. The computed average core flow rates at these instances

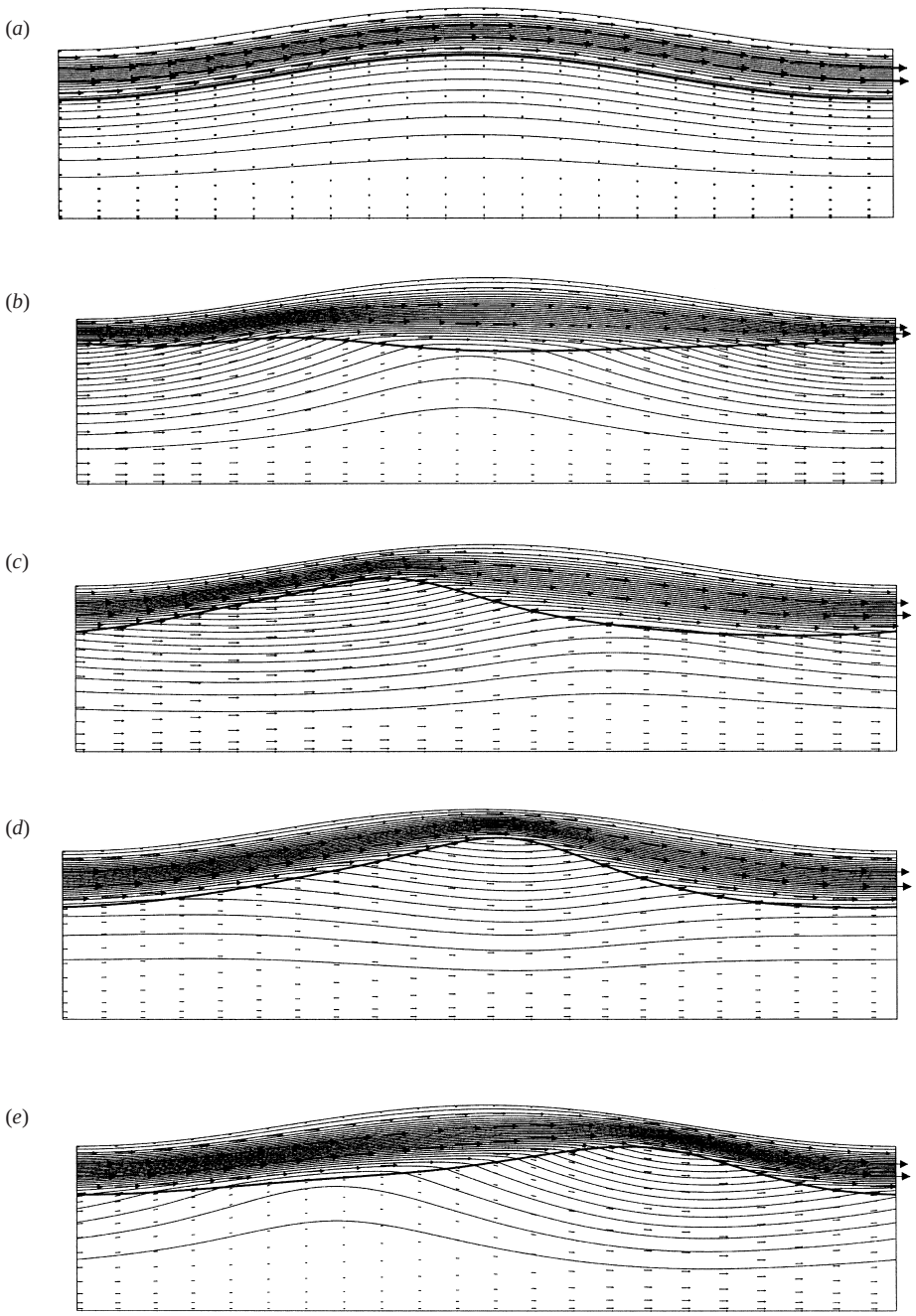

FIGURE 14. Flow fields that correspond to (*a*) the steady solution, (*b*) $t = 68.55$, (*c*) $t = 69.05$, (*d*) $t = 69.55$, (*e*) $t = 70.05$ $(\alpha, \Lambda, N, V, \mu, \rho, Re, W, F) = (0.8, 1, 1, 0.552, 0.00166, 1.09945, 0.1, 10.2, -23.9)$.

are found to be $\langle Q_1 \rangle = 0.783$, 0.789, 0.766 and 0.763, respectively, and no back flow of the annular fluid is observed. In fact, the core fluid drags the annular fluid more effectively here in both steady and periodic states, because of the increased viscosity of the latter. The computed values of the interfacial velocities are $\langle u_i \rangle = 3.442$, 3.441, 3.416 and 3.424, respectively. Comparing these figures and figures 9(*b*)–9(*e*),

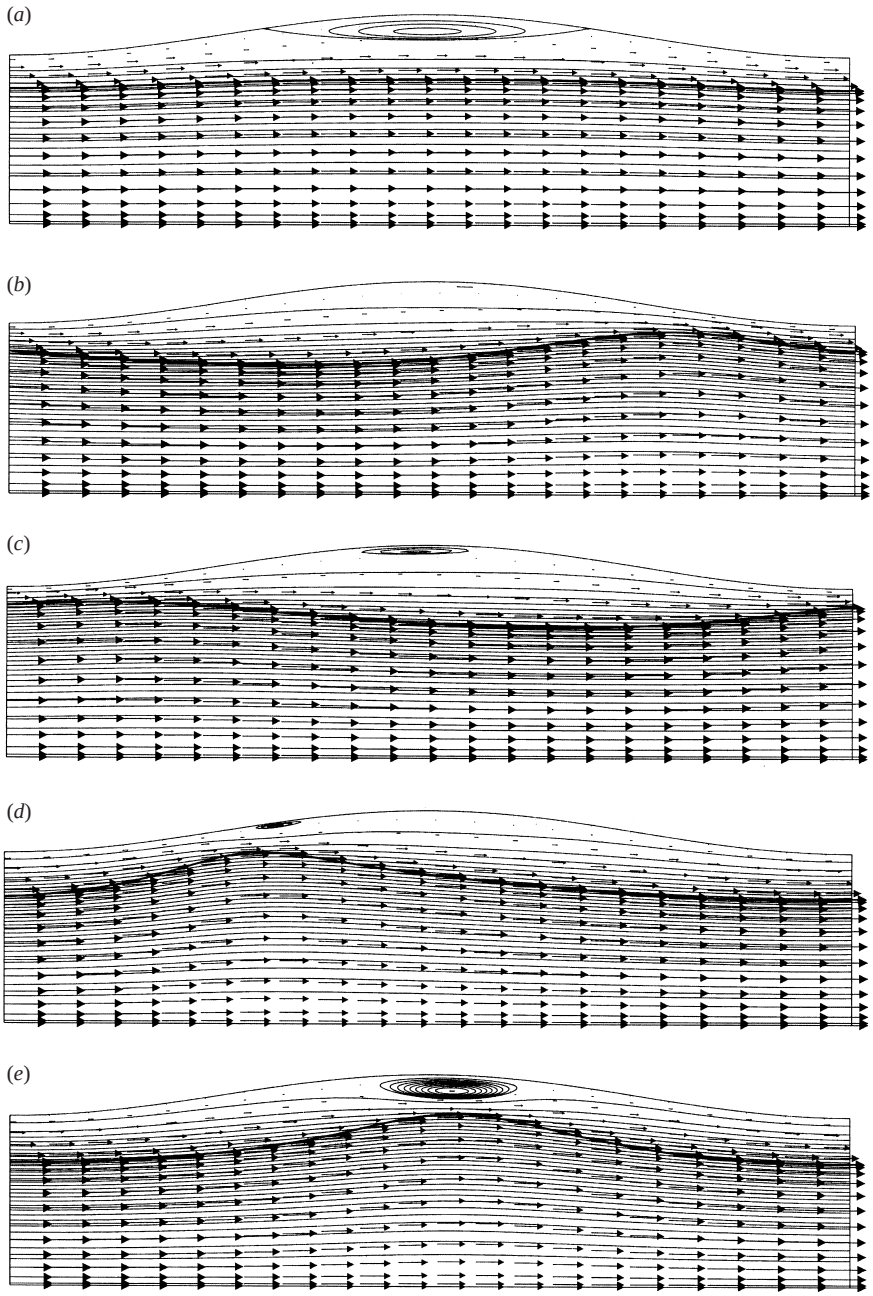

FIGURE 15. Flow fields that correspond to (*a*) the steady solution, (*b*) $t = 502.45$, (*c*) $t = 503.3$, (*d*) $t = 504.15$, (*e*) $t = 505$ $(\alpha, \Lambda, N, V, \mu, \rho, Re, W, F) = (0.8, 1, 1, 0.552, 0.0166, 1.09945, 0.1, 10.2, 23.9)$.

we conclude that the amplitude of the travelling waves is a decreasing function of the viscosity ratio. In previous linear stability analyses, Kouris & Tsamopoulos (2000, 2001*a*) have shown that CAF remains stable within a limited range of viscosity ratios that depends on the rest of the problem parameters. Thus, with increasing μ starting from very small values we are approaching the neutral stability boundary and thus we expect the decrease in the saturation amplitude of the bifurcating solution

and the decreased number of unstable eigenvalues reported earlier. We can also see that a vortex persists in the region occupied by the annular film in all times within one temporal period, but its position and strength are varied periodically in time without following closely the single crest of the interface. Additionally, the number of vortices of this type compared to that of case 4 is greatly reduced. This result is not unexpected, as the effective Reynolds number of the annular fluid is decreased here by an order of magnitude compared to that of case 4.

It is worth noting that the effect of the number of the unit cells that comprise the undulating tube has been investigated for this case also. More specifically, we have doubled the number of unit cells for case 7 and we have repeated the time integration. Our dynamic results, which are not shown for the sake of brevity, are exactly the same as those presented for the case with $N = 1$, validating in this way the use of a single cell. At this point, it is interesting to note the difference between the linear and the nonlinear temporal frequencies of cases 1–7. In cases 1–4 and 7, the linear frequency is greater than the nonlinear frequency and, more specifically, the greater the effect of gravity (cases 1–3), the larger the deviation between the frequencies, where gravity opposes the flow direction of the annular film. However, in cases 5 and 6, where gravity accelerates the annular fluid and surface tension is increased, the nonlinear frequency is greater than the linear frequency.

5. Small constriction ratio ($\alpha = 0.5$) with $\mu > 1$ (case 8)

In figures 16–18, we present the case with a fairly small ($\alpha = 0.5$) constriction ratio and the less viscous fluid is centrally located ($\mu = 2$). Hence, this case is above the upper neutral branch predicted by linear analysis (Kouris & Tsamopoulos 2001*a*). The two fluids are of equal density ($\rho = 1$) and, as a result, gravity does not enter the problem ($F = 0$). The constricted tube is composed of 2 unit cells ($N = 2$) and thus, the total length of the tube is approximately 12.5 times its maximum radius. The time integration has been initiated using the steady-state solution seeded with random disturbances of very small amplitude. The time evolution of the core flow rate can be seen in figure 16(*a*). The core flow rate at $t = 0$ and before measurable growth of the instability is $\langle Q_1 \rangle \sim 0.9984$, whereas after saturation it varies between the values $\langle Q_1 \rangle = 0.996$ and 1.001 and its time-averaged value is equal to $\{Q_1\} = 0.9984$. Apparently, the average core flow rate that corresponds to the time periodic solution is equal to the (unstable) steady solution. Concurrent flow occurs in both the linear and the nonlinear regime, but the flow rate of the annular fluid is very small ($0.002 \ll 1$). This is mainly caused by the fact that the core volume fraction used in this case is close to 1 ($V = 0.842$) and the small value of the constriction ratio creates large grooves inside which most of the annular fluid is trapped. Thus, only a small amount of the annular fluid is dragged by the core fluid, while the rest of it recirculates. This observation holds not only for the steady solution, but also for the time periodic solution, as it will be presented next. The mean value of the steady interfacial velocity equals $\langle u_i \rangle = 0.225$. Figure 16(*a*) shows a temporal oscillation of high frequency 4.488 that appears in spurts twice during each long period corresponding to the second, much lower frequency, 0.0583. The spurt that coincides with the step decrease in the core flow rate has larger amplitude than the other one. Linear theory predicts that the steady state solution is unstable with only one unstable eigenvalue (0.01159 ± 0.06381i). Apparently, the linear frequency is comparable and close to the nonlinear one, whereas the fast oscillation has no counterpart in the linear regime and, thus, it is produced by nonlinear interactions, as it will be discussed next.

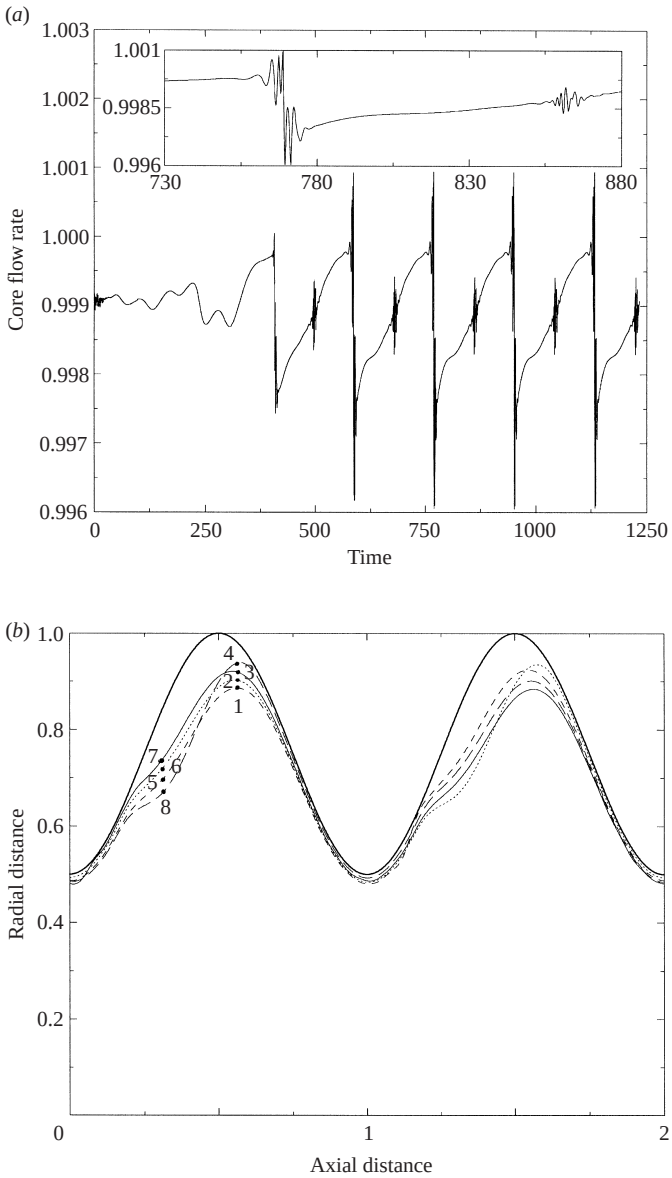

FIGURE 16. (*a*) Time evolution of the core flow rate and (*b*) instantaneous shapes of the interface, (----, $t = 1123.75$, $\cdots\cdots$, $t = 1151.75$, ——, $t = 1179.75$, – – –, $t = 1207.75$) $(\alpha, \Lambda, N, V, \mu, \rho, Re, W, F) = (0.5, 1, 2, 0.842, 2, 1, 11, 10, 0)$.

In figure 16(*b*), four instantaneous interfacial shapes, as well as the solid surface (thick line), can be seen. The times they were taken span the long temporal period. The common characteristic of these shapes is that the interface remains very close to the solid surface at the neck of the tube, whereas it becomes more deformed on the left-hand side of each unit cell as the two fluids enter the expanding portion of the tube. In these locations, a bulge in the interface arises periodically owing to the interaction of the interface with a vortex that is located in this region and then disappears. For the same reason, the deformed interface is shifted towards the right of

the mid-plane of the tube. It can be seen that, the maximum or the minimum of the crest of the interface in the left-hand unit cell is not attained simultaneously with the corresponding ones in the right cell. Focusing our attention now on only the left-hand unit cell, we observe that, as time evolves, the crest of the interface shifts upwards (points 1, 2 and 3) and, when it is maximized (point 4), it starts decreasing and finally reaches point 1 at the completion of each cycle. At the same times, the bulge of the interface is out-of-phase with the previous cycle, since it is slowly disappearing as the crest is increasing its amplitude, but reappears when the crest of the interface is maximized, see points 5, 6, 7 and 8. This wave attains its maximum amplitude in most of the expanding portion of the tube, and its minimum amplitude at its throat.

The flow fields that correspond to the steady solution, as well as to the time periodic solution, for the four time instances presented in figure 16(b) are shown in figures 17(a) and 17(b)–17(e), respectively. The distance between consecutive open and closed streamlines is constant and in the open ones it is equal to 0.025, whereas in the closed ones it is equal to 0.0001. Apparently, the flow fields that correspond to each of the unit cells presented in figure 17(a) are identical with each other, which is expected since the steady flow field is independent of the number of cells that comprise the computational domain. Figures 17(b)–17(e) demonstrate the fact that this symmetry in the steady-state solution breaks and a time-dependent solution is eventually established. Clearly, we observe that the two vortices that exist in the steady-state solution continue to exist in the time periodic solution, but now the intensity of each one varies in time. More specifically, when the intensity of the right-hand vortex attains its maximum value (figure 17c), the left-hand one attains its minimum and vice versa. By careful examination of figures 17(b)–17(e), we conclude that the flow field that occurs in the left-hand tube of figures 17(b) (17c) is the same as that in the right-hand tube of figure 17(d) (17e) and the flow field that occurs in the right-hand tube of figure 17(b) (17c) is the same as that in the left-hand tube of figure 17(d) (17e). The mean values of the interfacial velocities that correspond to figures 17(b)–17(e) are $\langle u_i \rangle = 0.267$, 0.208, 0.264 and 0.204, respectively. The resemblance of the interfacial velocity, $\langle u_i \rangle$, computed for the flow field shown in figure 17(b) (17c) with that of figure 17(d) (17e), respectively, is expected since these flow fields, apart from an axial translation by one unit cell, are the same. The mean interfacial velocity of the time periodic solution $\frac{1}{4}(0.267 + 0.208 + 0.264 + 0.204) = 0.235$ does not deviate appreciably from that of the steady interface which is equal to 0.225. Apparently, now that the more viscous fluid flows in the annulus, the velocity of the interface of the time periodic solution is greater than that of the steady solution. This increase in the velocity of the interface cannot be attributed to the effect of gravity, as in case 5. This observation is in accordance with the results presented in Kouris & Tsamopoulos (2002), where the nonlinear dynamics of the perfect CAF in a straight tube have been examined. In that case, it was shown that the velocity of the time dependent interface compared to that of the undisturbed interface is an increasing function of the viscosity ratio and when $\mu > 1$ ($\mu < 1$) the nonlinear interface is drifting faster (slower) than the steady one.

Figure 18 shows the evolution of the deviation, $R_1(t) - R_1$, of the instantaneous interface, $R_1(t)$, from its steady shape, R_1. The first snapshot corresponds to $t = 1119.75$ and the time difference between consecutive snapshots is $\Delta t = 4$. It is worth noting that the interface deviation, which is $O(10^{-2})$, attains its maximum value periodically and at axial distances 0.5 and 1.5, i.e. where the tube radius is maximized, while the

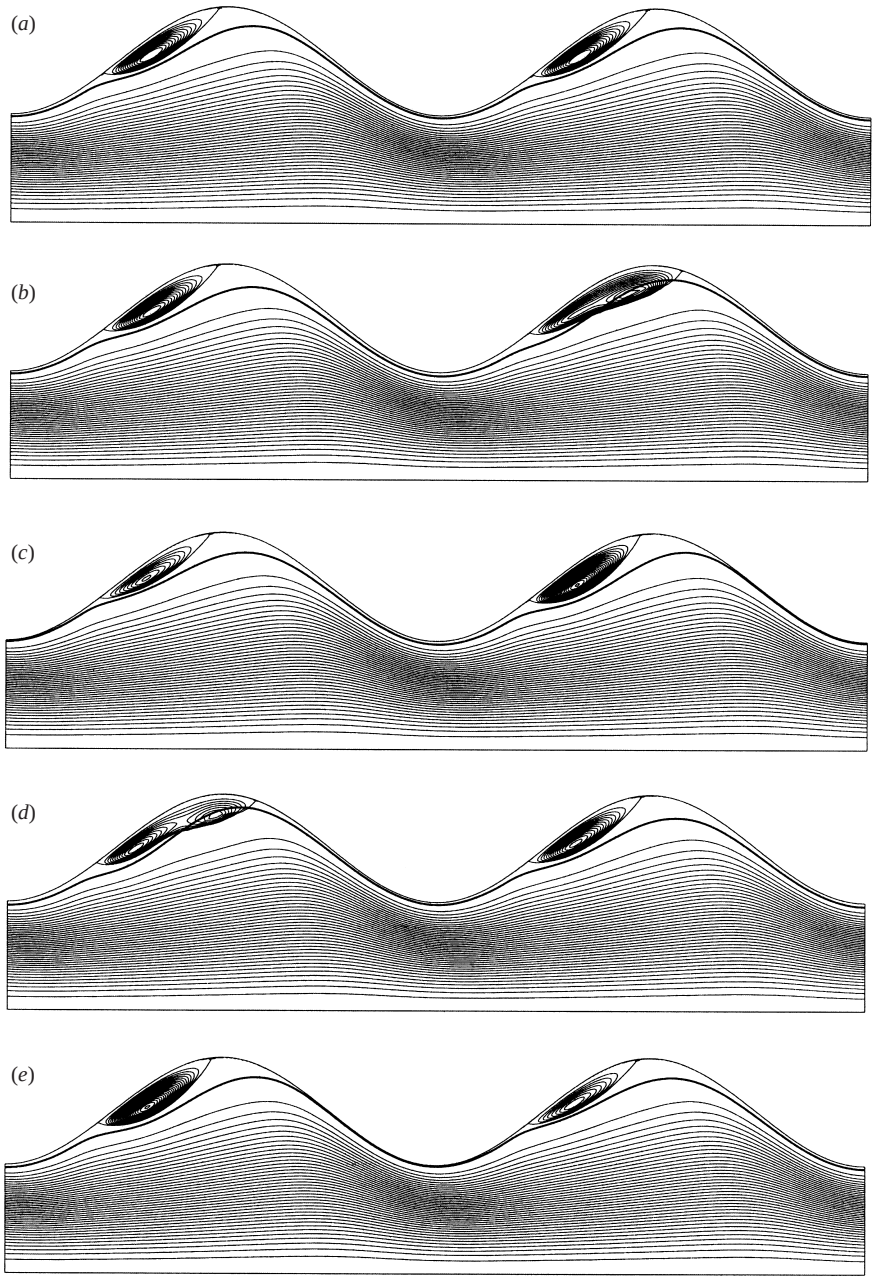

FIGURE 17. Flow fields that correspond to (*a*) the steady solution, (*b*) $t = 1123.75$, (*c*) $t = 1151.75$, (*d*) $t = 1179.75$, (*e*) $t = 1207.75$ $(\alpha, \Lambda, N, V, \mu, \rho, Re, W, F) = (0.5, 1, 2, 0.842, 2, 1, 11, 10, 0)$.

crests that are formed around these locations decrease in amplitude very fast. Close observation of this figure reveals the coexistence of a standing and a travelling wave. The standing wave gives rise to crests and when one crest attains its maximum value at axial distance 0.325, the next one attains its minimum value at 1.325, whereas the travelling wave, which is of smaller amplitude, is strangulated every time it goes through a tube throat. These two waves collide periodically. The low-frequency oscil-

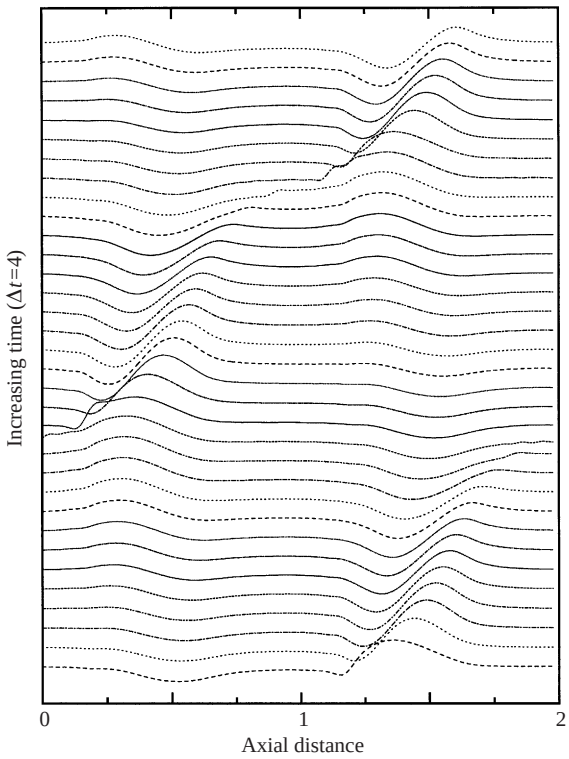

FIGURE 18. Time evolution of the interface deviation from the steady solution. The first snapshot corresponds to $t_1 = 1119.75$ and the time difference between consecutive one is $\Delta t = 4$. Time increases upwards $(\alpha, \Lambda, N, V, \mu, \rho, Re, W, F) = (0.5, 1, 2, 0.842, 2, 1, 11, 10, 0)$.

lation that can be seen in figure 16(a) is associated with the time that is required by the progressive wave to travel the whole domain, whereas the high-frequency oscillation is associated with the time that the stationary and the progressive waves interact. Ripples are generated because of their interaction and, thus, the core flow rate exhibits high-frequency oscillations. The two different types of wave are of the same period and, as a result, the progressive wave collides with the standing wave twice during the time it takes the travelling wave to cross the whole domain. Therefore, the time evolution of the core flow rate is disturbed by the high-frequency oscillation twice (figure 16a). Among all cases presented herein, only cases 7 and 8 require more than 1 unit cell to obtain a solution independent of N (4 and 2 cells, respectively). In particular, for case 8, it would be interesting to increase N further, something we have not pursued.

6. Comparison with experiments

De Santos, Melli & Scriven (1991) have carried out experiments in a single vertical water-wet axisymmetric constricted tube with water and air flowing concurrently and gravity pointing in the common flow direction of the two fluids. They have used tubes with a single constriction, the shapes of which were displaced hyperbolas. Their experiments have revealed certain flow regimes that parallel certain flow regimes in a packed bed. More specifically, they have reported that, in the case of continuous gas

and annular film flow, a standing wave develops just below the narrowest point of the tube and that the liquid film tends to bulge at this particular cross-section. As the water flow rate is increased further, the amplitude of the standing wave grows and eventually forms a water bridge trapping, at least temporarily, air and preventing its flow. The fluid properties, reported in Kolb *et al.* (1990), are $\hat{\mu}_1 = 1.8 \times 10^{-5}$ Pa s and $\hat{\rho}_1 = 1.2\,\mathrm{kg\,m^{-3}}$ for the air and $\hat{\mu}_2 = 9.3 \times 10^{-4}$ Pa s and $\hat{\rho}_2 = 10^3\,\mathrm{kg\,m^{-3}}$ for water, while the surface tension coefficient is equal to $\hat{T} = 0.07\,\mathrm{kg\,s^{-2}}$. De Santos *et al.* (1991) have introduced two different Reynolds numbers characterizing each phase Re_L and Re_G. If these are combined with the physical properties of the two fluids as well as the geometry of the tube (constriction ratio and maximum radius), the core to the total volumetric flow rate as well as our adopted characteristic velocity can be computed using the following equations:

$$\{Q_1\} = 1 + \frac{\mu Re_L}{\rho Re_G}, \quad \hat{W}_o = \frac{aRe_G}{4\{Q_1\}} \frac{\hat{\mu}_1}{\hat{\rho}_1 \hat{R}_{max}}. \tag{6.1}$$

Assuming that $\hat{R}_{max} = 2.4\,\mathrm{mm}$, $\hat{R}_{min} = 1.2\,\mathrm{mm}$, $\hat{L} = 29.4\,\mathrm{mm}$ (these parameter values are given in Melli *et al.* 1990) and $Re_L = 140$, $Re_G = 170$ (these parameter values are given in de Santos *et al.* 1991), we compute the following values of the dimensionless numbers: $(\alpha, \Lambda, \mu, \rho, Re, W, F, \{Q_1\}) = (0.5, 0.51, 51.67, 833.33, 11.39, 1247.2, -1971.79, 0.951)$. Assuming a single cell ($N = 1$), the only parameter that should be specified is the volume ratio V, instead of $\{Q_1\}$, as explained in § 2, although the experiment has been performed for fixed $\{Q_1\}$. Thus, we set $V = 0.926$. Another difference between the way the experiment has been performed and the way we simulate it is the periodic boundary conditions that we impose in the axial direction. As a result, we do not expect accurate replication of the experimental results. The time integration has been initiated using the steady solution that corresponds to the above dimensionless numbers with the steady interface disturbed randomly. Linear stability predicts that the steady solution is unstable with three unstable modes ($0.8035 \times 10^{-2} \pm 0.37840$i, $0.2228 \times 10^{-1} \pm 0.75611$i, $0.1304 \times 10^{-1} \pm 0.11375 \times 10^{1}$i). The instability saturates for time greater than 380 and the core flow rate varies between the values 0.9965 and 0.9978, with $\{Q_1\} = 0.997$. The temporal oscillation frequency in the nonlinear regime is found to be 0.754, i.e. very close to that of the most unstable mode predicted by the linear theory. We do not present the shape of the time-dependent interface, as the saturation amplitude of the instability is so small that the time-dependent and the time-independent solutions virtually coincide. It is worth mentioning that, for $V = 0.926$, the resulting mean value of the core flow rate is equal to 0.997 instead of the experimental value of 0.951. Although these two values seem to be close, when the corresponding ratios of the core to the annular flow rate are computed, they are found to be very different, because of a division by a very small number. In the former case this is equal to 332.3, whereas in the latter case it is 19.4.

For this reason, we have repeated the numerical experiment assuming a smaller value of the core volume fraction $V = 0.892$. In this way, the core fluid occupies a smaller portion of the tube, expecting in this way the resulting annular flow rate to be closer to the experimental value. For this value of V, the core flow rate that corresponds to the steady solution is equal to 0.991, whereas after saturation of the instability ($t > 117$), it varies between the values 0.979 and 0.997 with $\{Q_1\} = 0.991$. The linear and the nonlinear temporal oscillation frequencies as computed using dynamic simulation are equal to 2.371 and 2.435, respectively. Linear stability theory predicts that this steady solution is unstable, since there are four un-

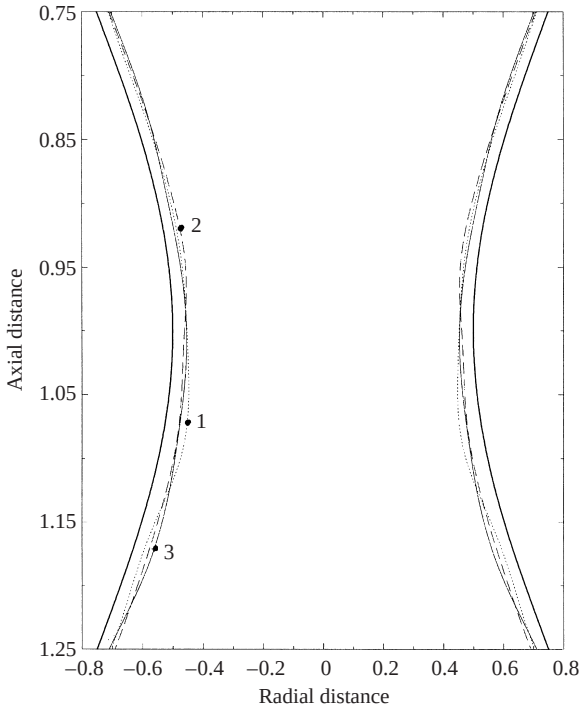

FIGURE 19. Instantaneous shapes of the interface of the time periodic solution (· · · · ·, $t = 146.65$, - - -, $t = 147.45$, ——, $t = 148.25$) $(\alpha, \Lambda, N, V, \mu, \rho, Re, W, F) = (0.5, 0.51, 1, 0.892, 51.67, 833.33, 11.39, 1247.2, -1971.79)$.

stable modes ($0.4518 \times 10^{-1} \pm 0.7977$i, $0.1404 \pm 0.1570 \times 10^{1}$i, $0.1936 \pm 0.2345 \times 10^{1}$i, $0.1419 \pm 0.3200 \times 10^{1}$i). Hence, the most unstable mode seems to be excited again. In figure 19, we present three different snapshots of the interface after saturation of the instability. The dotted line corresponds to $t = 146.65$, the dashed line to $t = 147.45$ and the solid line to $t = 148.25$. Close observation reveals that a bulge arises first in the dotted line at axial distance approximately 1.075 (point 1). This bulge is convected downstream and, owing to the periodicity, enters the computational domain from above and reappears at axial distance approximately 0.925 (point 2, on dashed line) and then at axial distance 1.17 (point 3, on solid line). Upon comparing these snapshots with the experimental photograph, we conclude that the predicted variation of the interface is smaller. The volumetric flow rate ratio of the core to the annular fluid for this case is equal to 110.1 and, although this value is smaller than that corresponding to the previous case (332.3), it is much larger than the experimental value (19.4). We have tried to reduce the imposed volume ratio further by setting $V = 0.876$ and we have repeated the calculations. In that case, however, after a short transient the computations terminate, and the interface becomes quite distorted. Therefore, with decreasing volume ratio, the travelling waves are more amplified, whereas they attain their largest amplitudes below the constriction, similar to what has been observed in the experiments. On the other hand, the fact that we cannot decrease the volume ratio further in order to approach the experimental operating conditions requires an explanation. We believe that this deviation results from the way the experiment has been performed and the boundary conditions that we use for simulating it. For example, if the steady flow is convectively unstable, something

we have every reason to believe (see figure 12 and related text), the finite length of the tube does not provide enough space for the instability to grow, but in our calculations the imposed periodicity in the axial distance provides sufficient distance for its development.

7. Conclusions

In this study, we have examined the nonlinear dynamics of the concentric, two-phase flow of two immiscible, Newtonian fluids in a circular tube of variable cross-section. The axisymmetric Navier–Stokes equations after being expressed in the streamfunction–vorticity variables have been discretized using a pseudo-spectral method in space and the implicit Euler method in time. The governing equations depend on nine dimensionless numbers and in addition to examining their effect on the time evolution of the CAF, we have also examined the effect of the condition used for initiating the time integration.

Assuming first that oil flows in the core and water in the annulus, we have varied the Reynolds number keeping constant the Galileo and the Ohnesorge number. In all examined cases, the inception and the subsequent saturation of the instability leads to flow regimes characterized by reduced oil flow rates and increased flow rates of the water compared to the steady solution. We have also demonstrated a case where countercurrent flow occurs in the linear regime and concurrent in the nonlinear one. We have shown that the presence of the constriction greatly modifies the well-known 'bamboo' waves that appear in straight tubes since the resulting waves travel with a non-constant wave speed and shape. More specifically, we have observed that, often but not always, the larger the amplitude of the wave, the smaller its velocity. The presence of the constriction forces the wave to deform as it travels downstream and when the wave is composed by at least two crests these appear to repel and attract each other periodically in time. We have also examined the effect of the initial condition and, when it is composed of the perfect steady CAF in addition to linear but random disturbances, the fluid/fluid interface exhibits chaotic behaviour similar to what has been observed in the case of the straight tube geometry.

The increase of the viscosity ratio and the decrease in the gravity parameter F lead to decrease in the saturation amplitude of the instability. In contrast, the increase in the surface tension parameter W causes increase in the saturation amplitude of the instability and in some cases can induce breakup of the interface leading in this way to discontinuous flow of the core fluid. We have simulated two different cases, which lead to breakup of the interface and are both characterized by large values of W. In the first one, where the more viscous fluid is centrally located, a neck of the interface is formed and two counter-rotating vortices appear to its left and to its right. These cause drainage of the core fluid forming a long neck. In the other case where the more viscous fluid is located in the annulus, the formation of a finger of annular fluid pointing towards the less viscous fluid is observed.

Finally, the constriction ratio has been decreased further in an attempt to simulate as closely as possible the flow regime in a trickle bed reactor. In this case, we have assumed values of the parameters so that water flows in the annulus and air in the core of the tube. Travelling waves develop onto their common interface, similar to what has been observed in experiments.

This work was partially supported under the EKBAN program (grant number 88) of the General Secretariat of Research and Technology of Greece and under the

EPEAEK program (grant number 51) of the Ministry of Education of Greece. The authors are also most thankful to Professor Y. Kevrekidis (Princeton University) for providing us with extra computer time.

REFERENCES

Aul, R. W. & Olbricht, W. L. 1990 Stability of a thin annular film in pressure-driven flow through a capillary. *J. Fluid Mech.* **215**, 585–599.

Bai, R., Chen, K. & Joseph, D. D. 1992 Lubricated pipelining: stability of core–annular flow. Part 5. Experiments and comparison with theory. *J. Fluid Mech.* **240**, 97–132.

Bai, R., Kelkar, K. & Joseph, D. D. 1996 Direct simulation of interfacial waves in a high-viscosity-ratio and axisymmetric core–annular flow. *J. Fluid Mech.* **327**, 1–34.

Drazin, P. G. & Reid, W. H. 1981 *Hydrodynamic Stability*. Cambridge University Press.

Frenkel, A. L., Babchin, A. J., Levich, B. G., Shlang, T. & Sivashinsky, G. I. 1987 Annular flows can keep unstable films from breakup: nonlinear saturation of capillary instability. *J. Colloid Interface Sci.* **115**, 225–233.

Hammond, P. S. 1983 Nonlinear adjustment of a thin annular film of viscous fluid surrounding a thread of another within a circular cylindrical pipe. *J. Fluid Mech.* **137**, 363–384.

Hickox, C. E. 1971 Instability due to viscosity and density stratification in axisymmetric pipe flow. *Phys. Fluids* **14**, 251–262.

Hooper, A. P. 1989 The stability of two superposed viscous fluids in a channel. *Phys. Fluids* A **1**, 1133–1142.

Hooper, A. P. & Boyd, W. G. C. 1983 Shear-flow instability at the interface between two viscous fluids. *J. Fluid Mech.* **128**, 507–528.

Joseph, D. D. & Renardy, Y. 1993 *Fundamentals of Two-Fluid Dynamics, Part II. Lubricated Transport, Drops and Miscible Fluids*. Springer.

Kawahara, T. 1983 Formation of saturated solitons in a nonlinear dispersive system with instability and dissipation. *Phys. Rev. Lett.* **51**, 381–383.

Kerchman, V. 1995 Strongly nonlinear interfacial dynamics in core–annular flows. *J. Fluid Mech.* **290**, 131–166.

Kolb, W. B., Melli, T. R., de Santos, J. M. & Scriven, L. E. 1990 Concurrent downflow in packed beds. Flow regimes and their acoustic signals. *Ind. Engng Chem. Res.* **29**, 2380–2389.

Kouris, Ch. 2000 Linear stability analysis and non-linear dynamics of the two-phase flow in straight and constricted tubes. PhD thesis, University of Patras.

Kouris, Ch., Dimakopoulos, Y., Georgiou, G. & Tsamopoulos, J. 2002 Comparison of spectral and finite element methods applied to the study of interfacial instabilities of the core–annular flow in an undulating tube. *Intl J. Numer Meth. Fluids* **39**, 41–73.

Kouris, Ch., Neophytides, S., Vayenas, C. G. & Tsamopoulos, J. 1998 Unsteady state operation of catalytic particles with constant and periodically changing degree of external wetting. *Chem. Engng Sci.* **53**, 3129–3142.

Kouris, Ch. & Tsamopoulos, J. 2000 Concentric core–annular flow in a circular tube of slowly varying cross section. *Chem. Engng Sci.* **55**, 5507–5525.

Kouris, Ch. & Tsamopoulos, J. 2001*a* Core–annular flow in a periodically constricted circular tube. Part 1. Steady state, linear stability and energy analysis. *J. Fluid Mech.* **432**, 31–68.

Kouris, Ch. & Tsamopoulos, J. 2001*b* Dynamics of axisymmetric core–annular flow I. The more viscous fluid in the core, bamboo waves. *Phys. Fluids* **13**, 841–858.

Kouris, Ch. & Tsamopoulos, J. 2002 Dynamics of axisymmetric core–annular flow II. The less viscous fluid in the core, saw tooth waves. *Phys. Fluids* **14**, 1011–1029.

Li, J. & Renardy, Y. 1999 Direct simulation of unsteady axisymmetric core–annular flow with high viscosity ratio. *J. Fluid Mech.* **391**, 123–149.

Melli, T. R., De Santos, J. M., Kolb, W. B. & Scriven, L. E. 1990 Concurrent downflow in networks of passages. Microscale roots of macroscale flow regimes. *Ind. Engng Chem. Res.* **29**, 2367–2379.

Papageorgiou, D. T., Maldarelli, C. & Rumschitzki, D. S. 1990 Nonlinear interfacial stability of core–annular film flows. *Phys. Fluids* A **2**, 340–352.

Preziosi, L., Chen, K. & Joseph, D. D. 1989 Lubricated pipelining: stability of core–annular flow. *J. Fluid Mech.* **201**, 323–356.

de Santos, J. M., Melli, T. R. & Scriven, L. E. 1991 Mechanics of gas–liquid flow in packed-bed contactors. *Annu. Rev. Fluid Mech.* **23**, 233–260.

Yiantsios, S. G. & Higgins, B. G. 1988 Linear stability of plane Poiseuille flow of two superposed fluids. *Phys. Fluids* **31**, 3225–3238.

Yih, C. S. 1967 Instability due to viscosity stratification. *J. Fluid Mech.* **27**, 337–352.